Neurobiology of Disease

TRPM2 and CaMKII Signaling Drives Excessive GABAergic Synaptic Inhibition Following Ischemia

Amelia M. Burch,[1] Joshua D. Garcia,[2] Heather O'Leary,[1] Ami Haas,[1] James E. Orfila,[3] Erika Tiemeier,[1] Nicholas Chalmers,[1] Katharine R. Smith,[2*] Nidia Quillinan,[1*] and Paco S. Herson[3*]

[1]Neuronal Injury & Plasticity Program, Department of Anesthesiology, University of Colorado School of Medicine, Aurora, Colorado 80045, [2]Department of Pharmacology, University of Colorado School of Medicine, Aurora, Colorado 80045, and [3]Department of Neurological Surgery, The Ohio State University College of Medicine, Columbus, Ohio 43210

Excitotoxicity and the concurrent loss of inhibition are well-defined mechanisms driving acute elevation in excitatory/inhibitory (E/I) balance and neuronal cell death following an ischemic insult to the brain. Despite the high prevalence of long-term disability in survivors of global cerebral ischemia (GCI) as a consequence of cardiac arrest, it remains unclear whether E/I imbalance persists beyond the acute phase and negatively affects functional recovery. We previously demonstrated sustained impairment of long-term potentiation (LTP) in hippocampal CA1 neurons correlating with deficits in learning and memory tasks in a murine model of cardiac arrest/cardiopulmonary resuscitation (CA/CPR). Here, we use CA/CPR and an in vitro ischemia model to elucidate mechanisms by which E/I imbalance contributes to ongoing hippocampal dysfunction in male mice. We reveal increased postsynaptic $GABA_A$ receptor ($GABA_AR$) clustering and function in the CA1 region of the hippocampus that reduces the E/I ratio. Importantly, reduced $GABA_AR$ clustering observed in the first 24 h rebounds to an elevation of GABAergic clustering by 3 d postischemia. This increase in GABAergic inhibition required activation of the Ca^{2+}-permeable ion channel transient receptor potential melastatin-2 (TRPM2), previously implicated in persistent LTP and memory deficits following CA/CPR. Furthermore, we find Ca^{2+}-signaling, likely downstream of TRPM2 activation, upregulates Ca^{2+}/calmodulin-dependent protein kinase II (CaMKII) activity, thereby driving the elevation of postsynaptic inhibitory function. Thus, we propose a novel mechanism by which inhibitory synaptic strength is upregulated in the context of ischemia and identify TRPM2 and CaMKII as potential pharmacological targets to restore perturbed synaptic plasticity and ameliorate cognitive function.

Key words: **cardiac arrest; E/I balance; $GABA_A$ receptors; global cerebral ischemia; inhibitory synapse; TRPM2**

Significance Statement

Excitatory/inhibitory (E/I) imbalance drives long-term disability in numerous central nervous system disorders, including cerebral ischemia. Previous studies indicated ischemia-induced hippocampal synaptic plasticity deficits contribute to long-term cognitive impairment, yet the mechanisms underlying hippocampal dysfunction are poorly defined. Here, we combine in vivo and in vitro approaches to demonstrate elevated $GABA_A$ receptor clustering and function contribute to a reduction in hippocampal E/I balance and deficits in long-term potentiation at delayed timepoints following ischemia. We further identify ongoing activation of the TRPM2 ion channel and Ca^{2+}-dependent kinase, CaMKII, are required for the ischemia-induced enhancement of GABAergic synaptic inhibition, highlighting promising new targets to improve postischemic long-term functional recovery.

Introduction

Hippocampal dysfunction occurs as a consequence of brain injury, leading to impairments in learning and memory. Notably, cerebral ischemia has profound effects on hippocampal function due to the high metabolic requirements of the hippocampus (Petito et al., 1987; Schmidt-Kastner and Freund, 1991; Neumann et al., 2013). Ischemic insults trigger numerous pathways including excitotoxicity, which drives neuronal demise via

Received Sept. 22, 2023; revised March 13, 2024; accepted March 18, 2024.

Author contributions: H.O'L., K.R.S., N.Q., and P.S.H. designed research; A.M.B., J.D.G., H.O'L., A.H., J.E.O., E.T., and N.C. performed research; A.M.B., J.D.G., H.O'L., A.H., and J.E.O. analyzed data; A.M.B. wrote the paper.

This work was supported by an NIH Predoctoral NRSA F31NS120422 and T32GM763540 (A.M.B.), R01NS046072 (N.Q. and P.S.H.), R01NS118786 (P.S.H), R01NS092645 (P.S.H.), and R01MH119154 (K.R.S.) R01MH128199 (K.R.S.) and an AHA Career Development Award (K.R.S.). J.D.G. was supported by Grant T32GM763540, an AHA Predoctoral Fellowship (19PRE34380542), and an NIH Blueprint Diversity Specialized Predoctoral to Postdoctoral Advancement in Neuroscience (D-SPAN) Award (FNS120640A). We thank Dr. Ulrich Bayer for the gift of tatCN19o peptide and Drs. Mark Dell'Acqua and Jacob Basak for critically reading the manuscript. Graphical abstract and OGD diagrams were created by BioRender.com.

*K.R.S., N.Q., and P.S.H. contributed equally to this work.

The authors declare no competing financial interests.

Correspondence should be addressed to Paco S. Herson at paco.herson@osumc.edu or Nidia Quillinan at nidia.quillinan@cuanschutz.edu.

https://doi.org/10.1523/JNEUROSCI.1762-23.2024

excessive glutamate release and resultant activation of AMPA- and NMDA-type glutamate receptors. Thus, considerable research efforts have concentrated on mitigating excitotoxic effects through NMDA and/or AMPA receptor blockade (Turski et al., 1998; Walters et al., 2005; Kostandy, 2012; Wu and Tymianski, 2018). While this neuroprotective approach effectively reduces neuronal cell death in animal models, clinical trials have shown limited improvement in long-term functional recovery in patients likely due to the narrow therapeutic window required for these therapies (Cheng et al., 2004; Wahlgren and Ahmed, 2004; Katz et al., 2022).

Neurorestoration is an alternative strategy that aims to restore neural circuits perturbed by neuronal injury, by enhancing synaptic function and plasticity in surviving neurons, allowing for treatment within a broader therapeutic timeframe (Azad et al., 2016; Escobar et al., 2019). Indeed, this strategy can be reliably tested in a murine model of global cerebral ischemia (GCI) and cardiac arrest/cardiopulmonary resuscitation (CA/CPR). Despite the completion of cell death processes within days of the initial insult, we observed sustained impairments of long-term potentiation (LTP) in surviving hippocampal neurons, correlating with learning and memory deficits post-CA/CPR (Orfila et al., 2014; Dietz et al., 2020). Further, we demonstrated that delayed inhibition of the Ca^{2+}-permeable, transient receptor potential melastatin-2 (TRPM2) ion channel reverses impairments in hippocampal LTP and hippocampal-dependent behavioral tasks (Dietz et al., 2020, 2021), implicating TRPM2 as a potential target for neurorestorative therapy. However, the precise molecular mechanisms underlying hippocampal dysfunction and the contribution of ongoing TRPM2 activity to LTP impairment remain elusive.

Extensive studies have emphasized the importance of maintaining a balance between excitatory and inhibitory (E/I) signaling for optimal neuronal function and induction of LTP mechanisms (Smith and Kittler, 2010; Vogels et al., 2011). Specifically, GABAergic synaptic inhibition plays a critical role in E/I balance by regulating circuit and neuronal excitability (Chiu et al., 2019). Further, prior work indicates that GABAergic inhibitory signaling directly impacts excitatory LTP (Steele and Mauk, 1999; Leao et al., 2012; Williams and Holtmaat, 2019; Udakis et al., 2020). In the context of cerebral ischemia, excitotoxic insult promotes rapid declustering of synaptic $GABA_A$Rs, subsequent elimination of inhibitory synapses, and neuronal cell death (Smith et al., 2012; Mele et al., 2014; Costa et al., 2016). Conversely, at delayed timepoints following the completion of cell death processes, there is accumulating evidence of excessive GABAergic function through overactivation of synaptic (phasic; Hiu et al., 2016) and extrasynaptic (tonic) $GABA_A$Rs (Clarkson et al., 2010; Carmichael, 2012; Orfila et al., 2019). However, the precise upstream mechanisms driving this enhancement and whether these pathways contribute to sustained synaptic plasticity and cognitive deficits remain poorly defined. In light of the established role of GABAergic inhibition in modulating excitatory synaptic plasticity, we tested the effect of ischemia on synaptic GABAergic inhibition and whether TRPM2 reverses LTP impairments via modulation of GABAA receptor ($GABA_A$R) function.

Here, we present data demonstrating a shift in the balance of E/I signaling in the hippocampus after CA/CPR. At acute timepoints, we found a decrease in $GABA_A$R clustering. However, in the postacute phase following the completion of cell death processes, we observed a sustained increase in postsynaptic inhibition, leading to a reduction in E/I balance. Using a combination of in vitro and in vivo approaches, we rigorously identified the TRPM2 ion channel as a mediator of augmented inhibitory function. We also provide compelling evidence that TRPM2 and Ca^{2+}/calmodulin-dependent protein kinase II (CaMKII) activations are necessary for the sustained enhancement of postsynaptic GABAergic inhibition, highlighting potential therapeutic targets to improve functional recovery following brain ischemia.

Materials and Methods

Key resources

For details of key resources/reagents used in the study, see Table 1.

Experimental model and subject details

Animals. All studies conformed to the requirements of the National Institutes of Health *Guide for the Care and Use of Laboratory Animals* and were approved by the Institutional Animal Care and Use subcommittee of the University of Colorado, Denver AMC. C57BL/6 mice were bred in house in the Animal Resource Center at the University of Colorado Anschutz Medical Campus and monitored regularly for health. Mice were weaned between postnatal days 21 and 28 (P21 and P28) and housed in microisolator cages on a 14:10 light/dark cycle with water and chow available *ad libitum*.

Cardiac arrest/cardiopulmonary resuscitation. Male mice that were approximately 8–12 weeks old were subjected to either cardiac arrest and cardiopulmonary resuscitation (CA/CPR) or sham procedures as described previously (Deng et al., 2017; Dietz et al., 2020). Briefly, mice were anesthetized with 3% isoflurane. Mice were intubated and connected to a mouse ventilator set to 160 breaths per minute. Cardiac function was monitored via electrocardiography, and pericranial temperature was maintained at 37.5°C ± 0.2°C using a water-filled coil. Asystolic cardiac arrest was induced by KCl injection via a jugular catheter. CPR began 6 min after induction of cardiac arrest, by slow injection of 0.5–1.0 ml of epinephrine (16 µg epinephrine/ml, 0.9% saline), chest compressions at a rate of ∼300 min^{-1}, and ventilation with 100% oxygen. If the return of spontaneous circulation could not be achieved within 3 min of CPR, resuscitation was terminated and the mouse was excluded from the study. After surgical procedures, mice were housed individually in microisolator cages on heating pads. Postsurgical care included daily saline injections (1 ml) and moist chow for 72 h. Investigators performed all experiments blind to the surgical procedure of the animal, with a separate investigator generating the code.

Dissociated hippocampal cultures. Primary hippocampal cultures were prepared as described previously (Crosby et al., 2019; Rajgor et al., 2020; Garcia et al., 2021). Briefly, the hippocampi from neonatal rat pups (P0–P1) were dissected and dissociated in papain. The isolated neurons were then seeded in MEM supplemented with 10% FBS and penicillin/streptomycin. Cells were plated at a density of 150,000–200,000 cells per 18 mm, #1.5 glass coverslip coated with poly-D-lysine. The MEM was replaced with Neurobasal (NB) media (GIBCO) supplemented with B27 (GIBCO) and 2 mM GlutaMAX 24 h after plating. The media was refreshed every 5 d before removing half of the existing media and replacing it with fresh NB media. To restrict the growth of actively dividing cells, mitotic inhibitors (uridine fluoro deoxyuridine) were introduced on Day 5. The cultures were maintained at 37°C with 5% CO_2 for a period of 13–14 d before conducting OGD experiments.

Method details

Hippocampal slice preparation. Hippocampal slices were prepared during 7 d postsurgical procedures. Mice were anesthetized with 3% isoflurane in an oxygen-enriched chamber and then transcardially perfused with oxygenated ice-cold artificial cerebral spinal fluid (aCSF) containing the following (in mM): 126 NaCl, 25 $NaHCO_3$, 12 glucose, 2.5 KCl, 2.4 $CaCl_2$, 1.3 $NaHPO_4$, and 1.2 $MgCl_2$. Horizontal slices (300µM) were cut in aCSF supplemented with 9 mM $MgSO_4$ and continuous oxygenation using a Vibratome 1200 (Leica) and transferred to a holding chamber containing aCSF warmed to 33°C. After 30 min, slices

Table 1. Key resources table

Reagent or resource	Source	Identifier
Antibodies		
$GABA_AR$-γ2 (imaging)	Synaptic Systems	Catalog #224 004; AB_10594245
Gephyrin (3B11; imaging)	Synaptic Systems	Catalog #147 111; AB_2619837
VGAT (rabbit; imaging)	Synaptic Systems	Catalog #131 003; AB_887869
MAP2 (mouse; imaging)	Synaptic Systems	Catalog #188 011; AB_2661868
Anti-guinea pig Alexa Fluor 568	Life Technologies	Catalog #11075; AB_141954
Anti-mouse Alexa Fluor 488	Life Technologies	Catalog #21202; AB_141607
Anti-rabbit Alexa Fluor 647	Life Technologies	Catalog #31573; AB_2536183
Gephyrin (WB)	Synaptic Systems	Catalog #147 111; AB_2619837
PhosphoCaMKII T286	PhosphoSolutions	Catalog #p1005-286; AB_2492051
CaMKII	BD Transduction Laboratories	Catalog #611293; AB_398819
Vinculin	Cell Signaling Technology	Catalog #13901
HRP-conjugated goat anti-mouse	Jackson ImmunoResearch	Catalog #115-035-174; AB_2338512
HRP-conjugated goat anti-rabbit	Thermo Fisher Scientific	Catalog #31460; AB_228341
Primers		
GABRG2	Thermo Fisher Scientific	Mm00433489_m1
GABRA1	Thermo Fisher Scientific	Mm00439046_m1
GABRB3	Thermo Fisher Scientific	Mm00433473_m1
Chemicals, reagents, and kits		
Picrotoxin	Tocris Bioscience	Catalog #1128
Qx314	Tocris Bioscience	Catalog #1014
DNQX	Tocris Bioscience	Catalog #0189
Clotrimazole	Sigma-Aldrich	Catalog #6019
Experimental models: organisms/strains		
Rat, Sprague Dawley Charles River Laboratories	Charles River Laboratories	RRID: RGD_734476
Mice, C57BL/6	Charles River Laboratories	
Software		
Prism 9	GraphPad	https://www.graphpad.com/scientific-software/prism/
ImageJ	NIH	https://imagej.nih.gov/ij/

recovered for an additional 30 min at room temperature (RT), prior to electrophysiology recordings.

Whole-cell patch-clamp electrophysiology. CA1 pyramidal neurons were visualized using infrared digital interference contrast optics under 63× magnification and patch-clamped in whole-cell configuration. Borosilicate glass recording electrodes were pulled with either a Narishige or Sutter P-97 Flaming/Brown electrode puller (Sutter Instrument) with a resistance of 2.5–4.0 MΩ. The recording solution was exchanged at a flow rate of approximately 2 ml per minute at RT. Responses were amplified and filtered at 5 kHz (MultiClamp 700B) and digitized at 20 kHz (Digidata 1440A and Clampex 10.7). No series resistance compensation nor junction potential corrections were performed. Access resistance was monitored by delivering a −5 mV voltage step, and any experiments in which access resistance was above 30 MΩ or changed >20% between the onset and completion of the experiment were not used for experimental analyses.

Excitatory/inhibitory balance experiments were conducted by recording excitatory postsynaptic currents (EPSCs) at −70 mV and inhibitory postsynaptic currents (IPSCs) at 0 mV from the same cell with an internal solution containing the following (in mM): 135 $CsMeSO_4$, 10 HEPES, 10 BAPTA, 5 Qx314, 4 Na_2ATP, 4 $MgCl_2$, and 0.3 NaGTP, at pH 7.25 with 1 M CsOH. Responses were evoked using a monopolar electrode in the stratum radiatum to stimulate Schaffer collateral-commissural (SCC) apical dendrites using a constant current source (Digitimer). The episodic mode was used to record EPSCs and IPSCs responses evoked every 20 s for a minimum of 2 min each. Spontaneous inhibitory postsynaptic currents (sIPSCs) were recorded at −60 mV in gap-free mode, with an internal solution containing the following (in mM): 140 CsCl, 10 NaCl, 10 HEPES, 5 EGTA, 0.5 $CaCl_2$, 2 MgATP, and 5 Qx314 in aSCF containing 10 μM DNQX to block AMPA currents (Banks et al., 1998). The EGTA and $CaCl_2$ in the internal solution were replaced with 10 mM BAPTA to examine the role of Ca^{2+} signaling in postsynaptic neuron sIPSCs following CA/CPR. To determine the role of CaMKII activity in postsynaptic neurons sIPSCs following CA/CPR, the internal solution was supplemented with 5 μM tatCN19o (Barcomb et al., 2015; a gift from KU Bayer). To assess the role of TRPM2 activation in inhibitory function, 2 μM tatM2NX (Cruz-Torres et al., 2020; Dietz et al., 2020) was bath applied for at least 20 min prior to and during recording. For clotrimazole (CTZ) experiments, the baseline was recorded for 3 min, and clotrimazole (20 μM; Verma et al., 2012) was perfused onto the slice for 12 min. Access resistance was monitored every 3 min. Recordings that exhibited >20% drift in access resistance were discarded. The final 3 min of clotrimazole recordings were used for statistical comparison to baseline.

Field electrophysiology. Hippocampal slices were placed in a heat-controlled interface chamber perfused with aCSF at a rate of 1.5 ml/min at 32°C. Responses were evoked using an insulated tungsten bipolar stimulating electrode placed in stratum radiatum to stimulate Schaffer collateral-commissural (SCC) and recorded with a glass electrode containing 150 mM NaCl placed in the distal dendrites of CA1 pyramidal cell layer. Analog field excitatory postsynaptic potentials (fEPSPs) were amplified (1,000×) and filtered through a preamplifier (Grass Model P511) 0.03 Hz to 1.0 kHz, digitized at 10 kHz and stored on a computer for later offline analysis (Datawave Technologies). The derivative (dV/dT) of the initial fEPSP slope was measured. The fEPSPs were adjusted to 50% of the maximum slope and test pulses were evoked every 20 s. Paired-pulse responses were recorded using a 50 ms interpulse interval (20 Hz) and expressed as a ratio of the slopes of the second pulse over the first pulse. Picrotoxin (5 mM; Costa and Grybko, 2005) was applied for at least 20 min during the acquisition of a stable fEPSP baseline. Following the baseline recording, picrotoxin was washed out with normal aCSF, and theta burst stimulation (TBS) was delivered, which included a train of four pulses delivered at 100 Hz in 30 ms bursts repeated 10 times with 200 ms interburst intervals. Following TBS, the fEPSP

was recorded for 60 min. The averaged 10 min slope from 50 to 60 min after TBS was divided by the average of the 10 min baseline (set to 100%) prior to TBS to determine the amount of potentiation. For time course graphs, normalized fEPSP slope values were averaged and plotted as the percent change from baseline.

Immunohistochemistry. Mice were anesthetized and transcardially perfused with ice-cold PBS followed by 4% paraformaldehyde (PFA). Whole brains were removed and postfixed in 4% PFA at 4°C overnight. After 24 h, brains were transferred to a glycerol and Sorenson's buffer cryoprotection solution for long-term storage. Frozen coronal sections were made using a sliding microtome, and slices were placed in a cryostorage solution containing phosphate buffer, ethylene glycol, polyvinylpyrrolidone, and sucrose and stored at 4°C until staining was performed. Free-floating sections were washed for 15 min (three times) in PBS at RT then blocked and permeabilized (5% BSA, 5% NGS, 0.5% Triton X-100, and 1× PBS) at RT for 5–6 h on a rocker. Slices were incubated with gephyrin (1:500 Synaptic Systems, mouse, 147011) and VGAT (1:1,000 Synaptic Systems, rabbit, 131003) antibodies in permeabilization solution overnight at 4°C on a rocker. Slices are washed for 20 min in PBS (four times) and incubated with appropriate secondary antibodies (1:1,000 Thermo Fisher Scientific, Alexa Fluor 488 and 568) for 2 h in a blocking solution. Prior to mounting with ProLong Gold, slices were washed for 20 min in PBS (four times).

Immunocytochemistry. Coverslips containing neuronal cultures were fixed in a 4% PFA solution consisting of 4% sucrose, 1× PBS, and 50 mM HEPES (pH 7.4) for 5 min at RT. After fixation, the cells were blocked in a solution containing 5% BSA, 2% normal goat serum (NGS), and 1× PBS at RT for 30 min. Staining for surface $GABA_AR$-γ2 subunit (1:500, Synaptic Systems, guinea pig, 224004) was performed under nonpermeabilized conditions in the blocking solution for 1 h at RT. Following the primary antibody incubation, coverslips were washed three times for 5 min each with 1× PBS. Subsequently, permeabilization was carried out using 0.5% NP-40 for 2 min, followed by blocking at RT for 30 min. Staining for gephyrin (1:600, Synaptic Systems, mouse, 3B11 clone, 147111) and VGAT (1:1,000, Synaptic Systems, rabbit, 131003) or MAP2 (1:1,000, Synaptic Systems, mouse, 188011) was performed in the blocking solution for 1 h, following by three 5 min washes with PBS. The coverslips were then incubated with appropriate secondary antibodies (1:1,000, Thermo Fisher Scientific, Alexa Fluor 488, 568, and 547). Coverslips were washed three times for 5 min and were then mounted on microscope slides using ProLong Gold mounting media (Thermo Fisher Scientific). For experiments requiring nonpermeabilizing conditions, the 0.5% NP-40 step was omitted.

Oxygen glucose deprivation (OGD) in neuronal culture. OGD was induced in DIV13–15 hippocampal neuronal cultures using a HEPES-buffered solution. The OGD-HEPES solution contained the following (in mM): 25 HEPES (pH 7.4), 140 NaCl, 5 KCl, 2 $CaCl_2$, 1 $MgCl_2$, and 10 sucrose (or supplemented with 10 mM glucose for control conditions). Prior to OGD treatment, the OGD-HEPES solution was placed in an anaerobic workstation at 37°C with a controlled atmosphere of 95% N_2 and 5% CO_2 (Bugbox Plus, Baker Co) for 24 h to allow for deoxygenation. Neuronal cultures were washed twice and incubated with OGD-HEPES solution in the anoxic chamber for 20 min. Reoxygenation was then initiated by replacing the OGD-HEPES solution with glucose-containing conditioned media and returning coverslips to an aerobic incubator. After 96 h in aerobic conditions, coverslips were fixed for immunocytochemistry. For the treatment conditions, coverslips were treated with various inhibitors for 1 h prior to fixation. The following inhibitors and concentrations were used (in μM): 20 CTZ, 2 tatM2NX, 2 tatScr, 5 tatCN19o, and 5 KN93. Control neurons were incubated at 37°C, 5% CO_2 with control-HEPES solution for 20 min and returned to conditioned media before fixation at the 96 h timepoint.

Protein fractionation and Western immunoblotting. Mice were anesthetized, followed by rapid decapitation and brain removal. The whole hippocampus was dissected and flash frozen and stored at −80°C until membrane fractionation was performed. Membrane fraction preparation was performed as described previously (Deng et al., 2017). The whole hippocampus was homogenized in ice-cold homogenization buffer containing the following (in mM) 10 Tris (pH7.4), 320 sucrose, 1 μM EDTA, and 1 μM EGTA, with phosphatase and protease inhibitors (Thermo Fisher Scientific) using glass homogenizers and a drill fitted with a pestle. Homogenates were then transferred to 1.5 ml Eppendorf tubes and centrifuged for 10 min at 1,000 × *g* at 4°C. The supernatant was collected and placed in a clean Eppendorf tube and centrifuged at 10,000 × *g* at 4°C. The supernatant was then removed, and the resulting pellet (P2) containing the membrane fraction was resuspended in 60 μl Neuronal Protein Extraction Reagent (Thermo Fisher Scientific). Protein concentrations were quantified using Pierce BCA Protein Assay Kit (Thermo Fisher Scientific) before diluting each sample in 5× SDS loading buffer to equal concentrations and heating to 95°C for 5 min. Protein separation was achieved by SDS-PAGE. Western immunoblotting was performed as described previously (Cruz-Torres et al., 2020). Proteins were transferred to PVDF membranes and using the following primary antibodies: CaMKII (1:1,000; CaMKII antibody, BD Transduction Laboratories, catalog #611293), phosphoCaMKII T286 (1:1,000; PhosphoSolutions, catalog #p1005-286), vinculin (1:1,000; Cell Signaling Technology, catalog #13901), and species appropriate secondaries (anti-mouse 1:5,000, Jackson ImmunoResearch; anti-rabbit, 1:5,000; Thermo Fisher Scientific).

Quantitative real-time PCR. For measurement of $GABA_AR$ subunit transcripts, CA1 isolates were harvested 7 d following sham and CA/CPR surgeries. RNA isolations and PCR were performed as previously described (Dietz et al., 2020). Briefly, per the manufacturer's instructions, RNA was isolated using the RNAqueous-4 PCR kit (Ambion). Approximately 0.5 mg of tissue was lysed in lysis buffer and total RNA was isolated and eluted from a column with 50 μl RNase-free elution buffer and further treated with Turbo DNase (Ambion). RNA (500 ng) was reverse transcribed to single-stranded cDNA using the iScript cDNA Synthesis Kit (Bio-Rad). Real-time PCR reactions using ssoFast PCR mastermix (Bio-Rad) were performed on the Bio-Rad CFX connect detection system and performed in triplicate using 50 ng of cDNA. Taqman (Thermo Fisher Scientific) primers were used to detect *GABRG2*, *GABRB3*, *GABRA1*, and 18 s transcripts. Cycle parameters used were 95°C for 10 min followed by 40 cycles of 95°C for 15 s and 60°C for 30 s. Relative expression levels were calculated using ΔΔCT as the ratio of the target gene to the housekeeping gene 18 s.

Image acquisition and data analysis

Confocal microscopy. Confocal images were acquired on a Zeiss Axio Observer Z1 upright microscope equipped with a Yokogawa CSU-X1 spinning disk unit; a 63× oil immersion objective using 2× digital zoom (Plan Apo/1.4 NA); an Evolve 512 EM-CCD camera (PhotoMetrics) with 16-bit range; and SlideBook 6.0. Alternatively, neurons were imaged using an Olympus FV1000 laser scanning confocal microscope, 60× oil immersion objective with 2× digital zoom, and Fluoview software (Olympus FluoView, FV10-ASW). Images on both microscopes were attained at 0.3 μm intervals (4 μm *Z*-stack projection). Cluster analysis was performed using ImageJ (NIH) by selecting regions of interest (ROIs) to differentiate between dendritic and somatic compartments. A user-based threshold was determined by sampling several images per condition across all conditions, and clusters were defined with a minimum size of 0.05 μm^2. For IHC experiments, the CA1 hippocampus was identified by VGAT staining of the pyramidal cell layer (PCL). ROIs captured both the PCL and stratum radiatum in the same frame, and different user-based thresholds were used for the cell bodies and dendrites. Density was calculated by dividing the number of clusters by the ROI area (per μm^2). A minimum of five animals per condition were utilized, with two slices per animal analyzed. Analysis was performed blind to surgical condition. For the in vitro experiments, ROIs were delineated by tracing along dendrites. The density of clusters was calculated by measuring the number of clusters divided by the length of the delineated dendrites (per 10 μm). A total of 30–36 neurons were analyzed per condition from three independent hippocampal preparations.

Experimental design and statistical analysis. All analyses were conducted blind to condition. The experimenter was additionally blind to condition when performing in vivo studies. A number of animals and cells are indicated in the figure legend. All data in the figures are presented as mean ± SEM. Statistical significance was determined using appropriate tests indicated in the figure legends. Statistical details for every dataset are provided in tables throughout the Results section. A p-value ≤0.05 was used to declare significance. All statistical analyses were performed on GraphPad Prism v9.4.

Results

E/I balance is disrupted following CA/CPR

To assess the effect of GCI on E/I balance, we employed patch-clamp electrophysiology to record evoked GABA (0 mV) and AMPA (−70 mV) responses from CA1 pyramidal neurons 7 d following CA/CPR or sham surgery (Fig. 1*A*), a postacute timepoint at which cell death processes have subsided and perturbations in synaptic function are reflective of the surviving network. The ratio of IPSC (GABA) to EPSC (AMPA) amplitude was greater in CA/CPR compared with sham, indicating increased synaptic inhibitory function relative to excitatory function (Fig. 1*B*; Table 2). This increase in inhibitory function following CA/CPR was observed with no difference in release probability in the CA/CPR group compared with sham as measured by the paired-pulse ratio of IPSCs (Table 3). No differences in EPSC release probability were also observed (Table 3). This suggests a potential enhancement of postsynaptic inhibitory function without a presynaptic effect, leading to an overall reduction in the E/I ratio. To determine the effect of increased inhibition on LTP deficits following CA/CPR, we performed extracellular field recordings in the CA1-Schaffer collateral pathway and recorded fEPSPs (Fig. 1*C*). We then treated hippocampal sections from CA/CPR mice with picrotoxin (5 mM; Costa and Grybko, 2005), a $GABA_AR$ pore blocker, to test the effect of GABAergic inhibition on LTP. Following theta burst stimulation (TBS), CA/CPR slices without treatment exhibited impaired LTP, consistent with previous reports (Fig. 1*D*; Table 2; Orfila et al., 2014, 2018; Dietz et al., 2020). However, treatment with picrotoxin restored LTP to sham levels (Fig. 1*D,E*; Table 2). No differences in the input–output curve (Table 4) and paired-pulse ratio

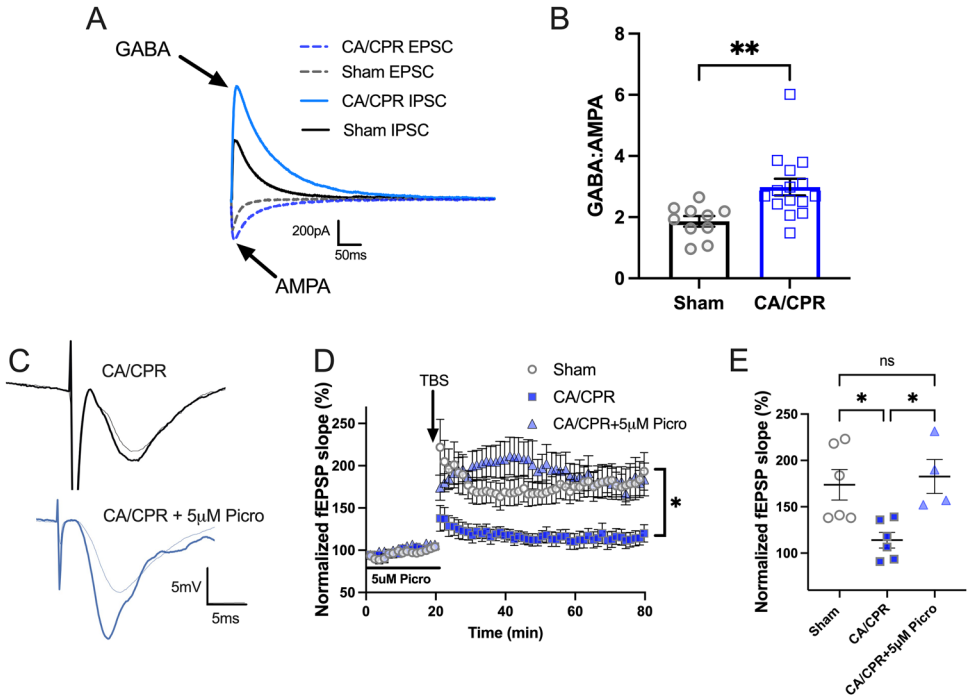

Figure 1. Excitatory/inhibitory balance is disrupted following CA/CPR. ***A***, Shown are representative traces for evoked EPSCs (solid) and IPSCs (dotted) recorded from the same CA1 hippocampal neurons of CA/CPR (blue) and sham (gray/black) mice. The AMPA eEPSCs are recorded with the neuron held at −70 mV, and GABA eIPSCs are recorded at 0 mV. ***B***, Quantification of the absolute value of the ratio of GABA eIPSC amplitude to the AMPA eEPSC amplitudes; $n = 11–15$ cells/3–5 animals per condition; unpaired t test. ***C***, Representative fEPSP traces from the stratum radiatum region of the CA1 hippocampus in CA/CPR slices without treatment (black) and CA/CPR slices (blue) treated with 5 μM picrotoxin during baseline. ***D***, LTP data presented as a percentage of the baseline, where the baseline is set at 100%. ***E***, Normalized slope of fEPSPs after theta burst stimulus; $n = 4–6$ slices/4–5 animals per condition; one-way ANOVA, Tukey's post hoc test. Values represent mean ± SEM. $*p < 0.05$, $**p < 0.01$.

Table 2. Statistical details for Figure 1

Statistical test	Test statistic, degrees of freedom	Post hoc test	Comparisons	p-value	Mean difference	95% confidence interval
Figure 1*B*—evoked E/I						
Unpaired t test	$t = 3.069$, df = 23	-	Sham vs CA/CPR	0.0054	1.118	0.3643 to 1.872
Figure 1*D*—LTP						
One-way ANOVA	$F_{(3,13)} = 5.566$	Tukey's multiple comparisons	CA/CPR vs sham	0.0208	−59.69	−110.3 to −9.121
			CA/CPR + picro vs sham	0.9082	8.983	−47.56 to 65.52
			CA/CPR vs CA/CPR + picro	0.0176	−68.67	−125.2 to −12.14

Table 3. Summary of passive membrane properties and paired-pulse ratio for whole-cell evoked E/I experiments, related to Figures 1, *A* and *B*, and 2, *G* and *H*

Whole-cell evoked E/I experiments—Figure 1, *A* and *B*

Cell parameter/measurement	Condition	Mean ± SEM	Comparisons	*p*-value (one-way ANOVA, Tukey's post hoc)	Mean difference	95% confidence interval
eIPSC paired-pulse ratio (100 ms interpulse interval)	Sham	0.7793 ± 0.05221	Sham vs CA/CPR	0.1023	−0.2550	−0.5506 to 0.04058
	CA/CPR	1.034 ± 0.08513	CA/CPR vs CA/CPR + CTZ	0.9291	0.04374	−0.2484 to 0.3358
	CA/CPR + CTZ	0.7355 ± 0.07451	Sham vs CA/CPR + CTZ	0.0170	0.2988	0.04679 to 0.5507
eEPSC paired-pulse ratio (50 ms interpulse interval)	Sham	1.215 ± 0.07285	Sham vs CA/CPR	0.8570	−0.08471	−0.4747 to 0.3053
	CA/CPR	1.300 ± 0.1327	CA/CPR vs CA/CPR + CTZ	0.4959	−0.1800	−0.5654 to 0.2054
	CA/CPR + CTZ	1.395 ± 0.07161	Sham vs CA/CPR + CTZ	0.7651	−0.09527	−0.4277 to 0.2371
Membrane resistance	Sham	98.63 MΩ ± 13.24 MΩ	Sham vs CA/CPR	0.4340	17.81	−16.91 to 52.53
	CA/CPR	80.82 MΩ ± 4.084 MΩ	CA/CPR vs CA/CPR + CTZ	0.1858	−26.24	−61.85 to 9.378
	CA/CPR + CTZ	124.9 MΩ ± 12.18 MΩ	Sham vs CA/CPR + CTZ	0.0060	−44.05	−76.82 to −11.27
Membrane capacitance	Sham	134.0 pF ± 7.480 pF	Sham vs CA/CPR	0.1406	−29.29	−65.99 to 7.403
	CA/CPR	163.3 pF ± 12.34 pF	CA/CPR vs CA/CPR + CTZ	0.6710	13.27	−24.37 to 50.92
	CA/CPR + CTZ	120.7 pF ± 9.284 pF	Sham vs CA/CPR + CTZ	0.0127	42.56	7.925 to 77.20

Table 4. Summary of fEPSP input–output slope and paired-pulse ratio for field electrophysiology experiments, related to Figure 1, *C–E*

Field LTP experiments—Figure 1, *C–E*

Measurement	Condition	Mean ± SEM	Comparisons	*p*-value (slope, simple linear regression; PPR, one-way ANOVA, Tukey's post hoc)	Mean difference	95% confidence interval
Input–output slope	Sham	1.778 ± 0.1784	Between all groups—are the slopes equal?	0.3090	N/A	1.413 to 2.142
	CA/CPR	2.021 ± 0.1058				1.805 to 2.236
	CA/CPR + picro	2.030 ± 0.06590				1.893 to 2.167
fEPSP –aired-pulse ratio (50 ms interpulse interval)	Sham	1.431 ± 0.04936	Sham vs CA/CPR	0.6839	0.05320	−0.1134 to 0.2198
	CA/CPR	1.377 ± 0.04536	CA/CPR vs CA/CPR + picro	0.3466	0.1021	−0.08413 to 0.2884
	CA/CPR + picro	1.275 ± 0.04131	Sham vs CA/CPR + picro	0.1082	0.1553	−0.03094 to 0.3416

(Table 4) were observed in the field recordings, suggesting enhanced postsynaptic $GABA_AR$ function contributes to LTP deficits at postacute timepoints following CA/CPR.

GABA sIPSC amplitude is increased following CA/CPR: inhibition of the TRPM2 ion channel rapidly restores sIPSC amplitude and E/I balance post-CA/CPR

To determine whether the increase in inhibitory function is pre- or postsynaptic, we recorded spontaneous IPSCs (sIPSCs) from CA1 neurons in CA/CPR and sham-operated mice and assessed amplitude, frequency, and decay kinetics (Fig. 2*A*; Table 5). The cumulative frequency of sIPSCs amplitude was shifted rightward in CA/CPR mice compared with sham-operated mice, indicating an overall increase in amplitude (Fig. 2*B*). Consistent with this, CA/CPR mice exhibited increased mean sIPSC amplitude compared with sham (Fig. $2C_1$; Table 6). No differences in mean frequency (Fig. $2C_2$; Table 6) or tau decay (Fig. $2C_3$; Table 6) were detected, suggesting the increase in inhibitory function is primarily postsynaptic.

Given the potential link between elevated GABAergic inhibition and LTP impairments in our experiments, we next asked whether TRPM2 inhibition, previously shown to restore LTP after CA/CPR (Dietz et al., 2020, 2021), potentially acts through postsynaptic GABAergic changes. To test this, we measured sIPSCs from CA1 neurons and bath applied tatM2NX (2 mM), a potent and specific TRPM2 inhibitor (Cruz-Torres et al., 2020), for at least 20 min prior to recording. CA/CPR slices treated with tatM2NX showed a reduction in sIPSC amplitude compared with CA/CPR slices without treatment, shifting the cumulative frequency of sIPSCs amplitude leftward (Fig. 2*B*). The mean amplitude was also reduced in tatM2NX-treated CA/CPR slices compared with slices without treatment (Fig. $2C_1$; Table 6). No differences in mean frequency (Fig. $2C_2$; Table 6) or tau decay (Fig. $2C_3$; Table 6) were detected across all conditions.

We then wanted to determine whether TRPM2 inhibition can *rapidly* reverse the CA/CPR-induced increase in amplitude within the same cell. We patched CA1 neurons from sham and CA/CPR mice and measured sIPSC amplitude, frequency, and tau decay before and after bath application of clotrimazole (CTZ, 20 mM), a fast-acting TRPM2 pore blocker (Table 5; Hill et al., 2004). CA/CPR slices treated with CTZ shifted the cumulative frequency of sIPSC amplitude leftward (Fig. 2*E*), indicating CTZ treatment restored sIPSC amplitude to sham levels. TRPM2 inhibition by CTZ rapidly reduced the CA/CPR-induced increase in sIPSC mean amplitude (Fig. $2F_1$; Table 6). Surprisingly, we observed a reduction in mean frequency in CA/CPR slices following bath application of CTZ (Fig. $2F_2$; Table 6). This was likely an off-target effect as the more specific TRPM2 inhibitor, tatM2NX, had no effect on frequency (Fig. $2C_2$; Table 6). However, consistent with the tatM2NX data, no differences were detected in tau decay across all conditions (Fig. $2F_3$; Table 6). These data suggest the increase in GABAergic function observed following CA/CPR is primarily postsynaptic and can be rapidly reversed following TRPM2 ion channel inhibition.

We next tested whether TRPM2 blockade would also reverse the CA/CPR-induced increase in the GABA:AMPA ratio shown in Figure 1*B*. To assess this, we again recorded evoked GABA (0 mV) and AMPA (−70 mV) responses from CA1 pyramidal neurons 7 d following CA/CPR and bath applied CTZ (20 mM; Fig. 2*G*). As predicted, CTZ treatment restored the GABA:AMPA ratio to sham levels (Fig. 2*H*; Table 6). Taken together, these findings indicate ongoing TRPM2 activity increases

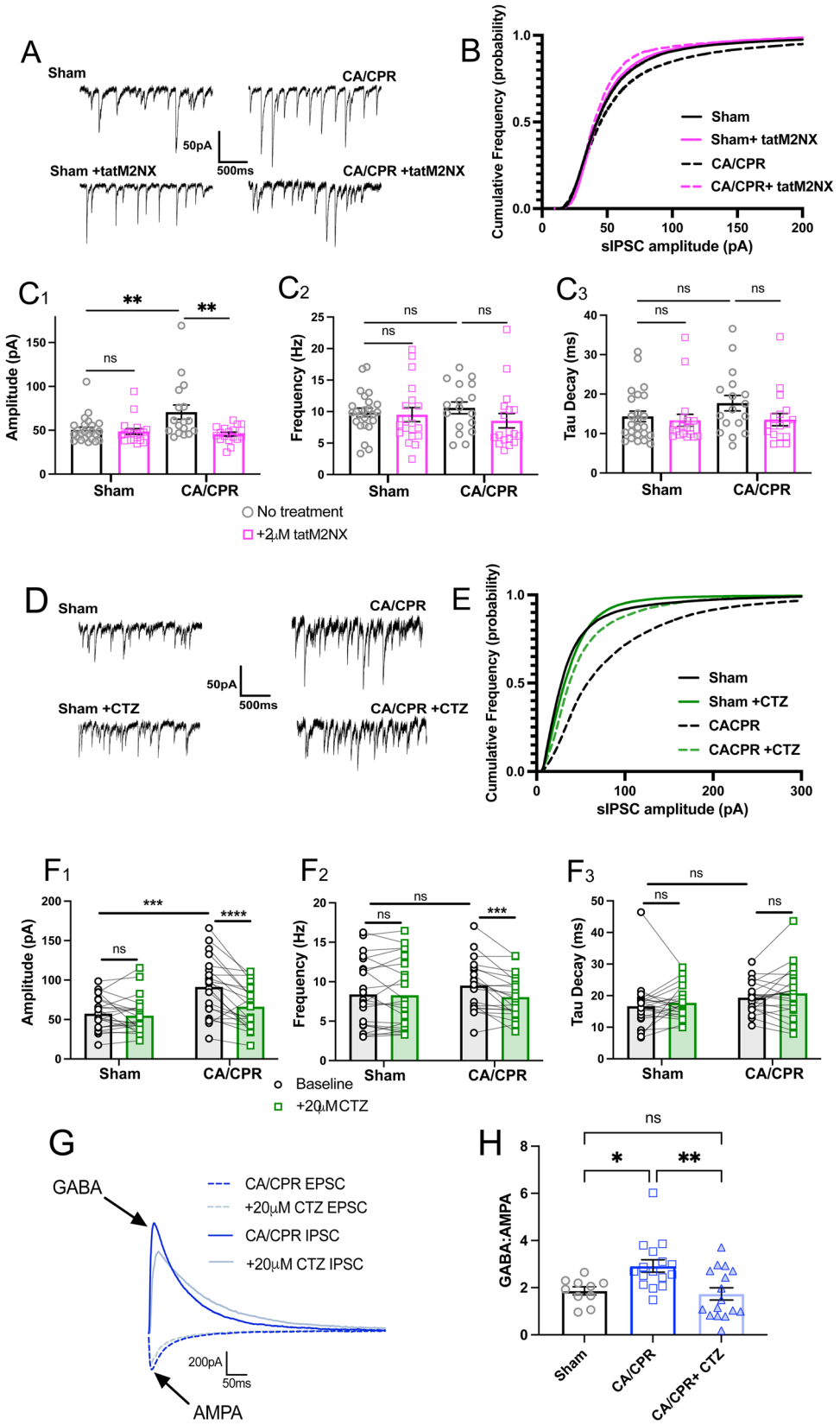

Figure 2. GABA sIPSC amplitude is increased following CA/CPR. TRPM2 ion channel inhibition rapidly restores sIPSC amplitude and E/I balance post-CA/CPR. ***A***, Representative traces from sham (top, left), sham with 2 μM tatM2NX bath applied (bottom, left), CA/CPR (top, right), CA/CPR with bath applied tatM2NX (bottom right) of whole-cell voltage-clamp recordings of sIPSC events recorded from CA1 pyramidal neurons in acute hippocampal slices using CsCl based internal solution holding at −60 mV. ***B***, Cumulative frequency distribution of sIPSC amplitude from sham cells (black, solid), sham + tatM2NX (black, dotted), CA/CPR (pink, solid), CA/CPR + tatM2NX (pink, dotted). ***C***, Mean amplitude (1), frequency (2), and tau decay (3) kinetics were measured from sIPSC events in different cells from sham and CA/CPR operated mice with and without bath application of tatM2NX; $n = 18–24$ cells/8–10 animals per condition; one-way ANOVA, Tukey's post hoc test. ***D***, Representative traces from sham (top, left), sham after clotrimazole (CTZ) from the same cell (bottom, left), CA/CPR (top, right), CA/CPR after CTZ from the same cell (bottom, right). ***E***, Cumulative frequency distribution of sIPSC amplitude from CA/CPR (black, dotted) following treatment with CTZ (20 mM) in the same cell (green, dotted). ***F***, Mean amplitude (1),

Table 5. Summary of amplitude, frequency, tau decay of sIPSCs for all conditions tested, related to Figures 2 and 8

Internal solution	Condition	Mean amplitude ± SEM (pA)	Mean frequency ± SEM (Hz)	Mean decay ± SEM (ms)	*N* (mice)	*n* (cells)
Population studies (different cells patched for drug conditions)						
CsCl	Sham	50.55 ± 3.021	9.864 ± 0.6820	14.34 ± 1.328	8	24
	Sham + tatM2NX	48.63 ± 3.252	9.519 ± 1.109	13.36 ± 1.528	12	19
	CA/CPR	70.75 ± 8.107	10.60 ± 0.9341	17.70 ± 1.955	11	17
	CA/CPR + tatM2NX	45.608 ± 2.207	8.553 ± 1.154	13.55 ± 1.550	10	18
Paired studies (same cell before and after drug application)						
CsCl	Sham	57.48 ± 4.498	8.389 ± 0.9211	16.66 ± 1.681	9	22
	Sham + CTZ	54.87 ± 4.923	8.298 ± 0.9358	17.73 ± 1.098		
	CA/CPR	91.24 ± 8.188	9.504 ± 0.701	19.34 ± 1.073	11	21
	CA/CPR + CTZ	66.25 ± 6.011	8.061 ± 0.5825	20.74 ± 1.794		
BAPTA	Sham	78.98 ± 10.29	7.507 ± 0.8206	18.96 ± 1.931	4	10
	Sham + CTZ	66.16 ± 7.021	6.677 ± 0.6352	15.46 ± 0.5528		
	CA/CPR	66.45 ± 6.998	8.898 ± 0.8444	19.09 ± 1.387	7	10
	CA/CPR + CTZ	57.87 ± 7.862	8.131 ± 0.6292	18.94 ± 1.146		
tatCN19o	Sham	67.29 ± 11.14	7.327 ± 1.021	22.88 ± 2.668	5	9
	Sham + CTZ	76.05 ± 11.2	8.143 ± 1.187	17.22 ± 1.909		
	CA/CPR	65.56 ± 8.538	7.664 ± 0.8301	18.8 ± 1.838	4	9
	CA/CPR + CTZ	78.18 ± 19.51	7.73 ± 0.8476	18.45 ± 2.192		

postsynaptic GABAergic function, resulting in disrupted E/I balance after CA/CPR.

CA/CPR induces a persistent increase in the clustering and density of gephyrin

We next investigated the mechanisms underlying the increase in inhibitory synaptic function driven by TRPM2 following CA/CPR. The increase in sIPSC amplitude suggests more postsynaptic receptor clustering at the synapse and a larger postsynaptic domain. To test this, we performed immunohistochemistry 7 d following sham and CA/CPR procedures and stained for the postsynaptic inhibitory scaffold protein, gephyrin, and the presynaptic inhibitory synapse marker, vesicular GABA transporter (VGAT; Fig. 3*A,B*). There was no difference in VGAT cluster area nor density between CA/CPR and sham in either the stratum radiatum (Fig. 3*C*; Table 7) or the stratum pyramidale (Fig. 3*D*; Table 7). In contrast, we observed an increase in gephyrin cluster density in the stratum radiatum (Fig. 3*C*; Table 7). In the stratum pyramidale, both gephyrin cluster area and density were increased in CA/CPR mice compared with sham (Fig. 3*D*; Table 7). These changes in postsynaptic GABAergic components were not due to altered gephyrin protein expression (Fig. 4*A,B*; Table 8) or altered transcription of various $GABA_AR$ subunits (Fig. 4*C,E*; Table 8). These findings align well with our electrophysiology data, suggesting CA/CPR enhances postsynaptic GABAergic function through increased receptor density, which can be rapidly reversed without affecting presynaptic inhibitory function.

OGD induces a persistent increase in the clustering and density of postsynaptic GABAergic proteins

To directly visualize $GABA_ARs$ and interrogate the mechanisms contributing to the enhancement of synaptic $GABA_AR$ clustering, we extended our studies to a well-established in vitro model of GCI (Arancibia-Carcamo et al., 2009; Smith et al., 2017; Garcia et al., 2021). We exposed dissociated hippocampal neurons to 20 min oxygen–glucose deprivation (OGD) followed by reoxygenation and fixed the neurons at varying timepoints to mimic the delayed 7 d timepoint we analyzed post-CA/CPR (Fig. 5*A*). To assess inhibitory synaptic size and postsynaptic receptor clustering, we immunostained for gephyrin, surface $GABA_ARs$ (γ2 subunit), and VGAT and evaluated cluster area and density of these markers in dendrites of pyramidal neurons using confocal microscopy (Fig. 5*B*). We observed a decrease in cluster area and density of all synaptic GABAergic components 24 h post-OGD, consistent with prior work showing an acute loss of GABAergic synapses (Garcia et al., 2021). However, by 48 h, these measurements were no different from control levels. By 72 and 96 h, both the cluster area (Fig. 5*C,E*; Table 9) and density (Fig. 5*F,H*; Table 9) increased for all synaptic GABAergic components. The increase in the presynaptic marker, VGAT, was unexpected given the in vivo CA/CPR data showed no changes in VGAT clustering (Fig. 5*C,D*; Table 7) or a presynaptic functional effect (Table 6). Despite this discrepancy, both postsynaptic markers exhibited an acute reduction in clustering followed by an increase in the chronic phase, consistent with the in vivo results shown prior (Fig. 3). To ensure the nonpermeabilization protocol used for these experiments reliably labeled the surface $GABA_ARs$, we stained for all three GABAergic markers under nonpermeabilizing (Fig. 6*A*) and permeabilizing conditions (Fig. 6*B*). As expected, we observed robust $GABA_AR$ staining under nonpermeabilizing conditions, while immunostaining for gephyrin and VGAT is notably absent due to lack of antibody access to cytoplasmic epitopes without permeabilization (Fig. 6*A*). Staining for all three GABAergic markers is present under permeabilizing conditions (Fig. 6*B*), suggesting the nonpermeabilization protocol used here for surface $GABA_AR$ staining is reliable. Finally, to ensure cell membrane integrity was not

←

frequency (2), and tau decay (3) kinetics were measured from sIPSC events in the same cell before and after bath application of CTZ from sham and CA/CPR operated mice; $n = 21–22$ cells/9–11 animals per condition; two-way ANOVA with repeated measures, Sidak's post hoc test. ***G***, Shown are representative traces for evoked EPSCs (solid) and IPSCs (dotted) recorded from the same CA1 hippocampal neurons of CA/CPR (blue) and CA/CPR with CTZ treatment (gray) mice. The AMPA eEPSCs are recorded with the neuron held at −70 mV, and GABA eIPSCs are recorded at 0 mV. ***H***, Quantification of the absolute value of the ratio of GABA eIPSC amplitude to the AMPA eEPSC amplitudes; $n = 11–15$ cells/3–5 animals per condition; unpaired *t* test. Sham and CA/CPR data from Figure 1*B* was used to compare the CA/CPR + CTZ group. Values represent mean ± SEM. $*p < 0.05$, $**p < 0.01$, $***p < 0.001$, $****p < 0.0001$.

Table 6. Statistical details for Figure 2

Statistical test	Test statistic, degrees of freedom, *p*-value (of interaction if two-way)	Post hoc test	Comparisons	*p*-value	Mean difference	95% confidence interval
Figure 2*C*$_1$—amplitude tatM2NX						
One-way ANOVA	$F_{(3,74)} = 6.002$	Tukey's multiple comparisons	Sham vs Sham + tatM2NX	0.9884	1.924	−13.78 to 17.63
			Sham vs CA/CPR	0.0086	−20.20	−36.42 to −3.988
			Sham vs CA/CPR + tatM2NX	0.8533	4.866	−11.08 to 20.81
			Sham + tatM2NX vs CA/CPR	0.0058	−22.13	−39.20 to −5.050
			Sham + tatM2NX vs CA/CPR + tatM2NX	0.9675	2.942	−13.88 to 19.77
			CA/CPR vs CA/CPR + tatM2NX	0.0016	25.07	7.770 to 42.37
Figure 2*C*$_2$—frequency tatM2NX						
One-way ANOVA	$F_{(3,74)} = 0.7159$	Tukey's multiple comparisons	Sham vs Sham + tatM2NX	0.9934	0.3449	−3.066 to 3.756
			Sham vs CA/CPR	0.9468	−0.7345	−4.256 to 2.787
			Sham vs CA/CPR + tatM2NX	0.7528	1.311	−2.153 to 4.775
			Sham + tatM2NX vs CA/CPR	0.8699	−1.079	−4.788 to 2.629
			Sham + tatM2NX vs CA/CPR + tatM2NX	0.8987	0.9661	−2.688 to 4.620
			CA/CPR vs CA/CPR + tatM2NX	0.4843	2.045	−1.712 to 5.802
Figure 2*C*$_3$—tau decay tatM2NX						
One-way ANOVA	$F_{(3,74)} = 0.2243$	Tukey's multiple comparisons	Sham vs Sham + tatM2NX	0.9674	0.9779	−4.609 to 6.564
			Sham vs CA/CPR	0.4237	−3.362	−9.129 to 2.405
			Sham vs CA/CPR + tatM2NX	0.9828	0.7944	−4.878 to 6.467
			Sham + tatM2NX vs CA/CPR	0.2463	−4.340	−10.41 to 1.734
			Sham + tatM2NX vs CA/CPR + tatM2NX	0.9998	−0.1835	−6.167 to 5.800
			CA/CPR vs CA/CPR + tatM2NX	0.2932	4.156	−1.996 to 10.31
Figure 2*F*$_1$—amplitude CTZ						
Two-way ANOVA	$F_{(1,19)} = 7.204$, $p = 0.0147$	Sidak's multiple comparisons	Sham − CA/CPR Baseline	0.0003	−33.76	−53.16 to −14.37
			Sham − CA/CPR Post-CTZ	0.3355	−11.39	−30.78 to 8.011
			Baseline − post-CTZ Sham	0.8133	2.608	−7.906 to 13.12
			Baseline − post-CTZ CA/CPR	<0.0001	24.99	14.23 to 35.75
Figure 2*F*$_2$—frequency CTZ						
Two-way ANOVA	$F_{(1,19)} = 3.646$, $p = 0.0714$	Sidak's multiple comparisons	Sham − CA/CPR Baseline	0.5523	−1.115	−3.713 to 1.482
			Sham − CA/CPR Post-CTZ	0.9730	0.2374	−2.360 to 2.835
			Baseline − post-CTZ Sham	0.9588	0.09066	−0.7225 to 0.9038
			Baseline − post-CTZ CA/CPR	0.0005	1.443	0.6111 to 2.276
Figure 2*F*$_3$—tau decay CTZ						
Two-way ANOVA	$F_{(1,19)} = 0.1366$, $p = 0.7158$	Sidak's multiple comparisons	Sham − CA/CPR Baseline	0.3522	−2.676	−7.344 to 1.991
			Sham − CA/CPR Post-CTZ	0.2696	−3.012	−7.680 to 1.655
			Baseline − post-CTZ Sham	0.6582	−1.072	−4.095 to 1.952
			Baseline − post-CTZ CA/CPR	0.5062	−1.408	−4.502 to 1.687
Figure 2*H*—evoked E/I						
One-way ANOVA	$F_{(2,39)} = 7.050$	Tukey's multiple comparisons	Sham vs CA/CPR	0.0242	−1.055	−1.991 to −0.1185
			Sham vs CA/CPR + CTZ	0.9416	0.1270	−0.8091 to 1.063
			CA/CPR vs CA/CPR + CTZ	0.0033	1.182	0.3607 to 2.003

compromised by the OGD stimulus, we stained for the somatodendritic marker, MAP2, and found no evidence of membrane instability after 20 min OGD compared with the control condition (Fig. 6*C*). The GABAergic synaptic markers used for our study were also sufficient to delineate dendrites as we observed a similar increase in $GABA_AR$ cluster area and density using MAP2 as a guide for dendritic analysis (Fig. 6*D*; Table 10). Thus, we utilized this optimized in vitro protocol, specifically the 96 h timepoint, to investigate the mechanism of TRPM2-mediated postsynaptic GABAergic enhancement.

The TRPM2 ion channel mediates the OGD-induced increase in clustering of postsynaptic GABAergic components

We next investigated whether TRPM2 activation affects the density of postsynaptic GABAergic proteins following OGD. We subjected hippocampal neurons to 20 min OGD

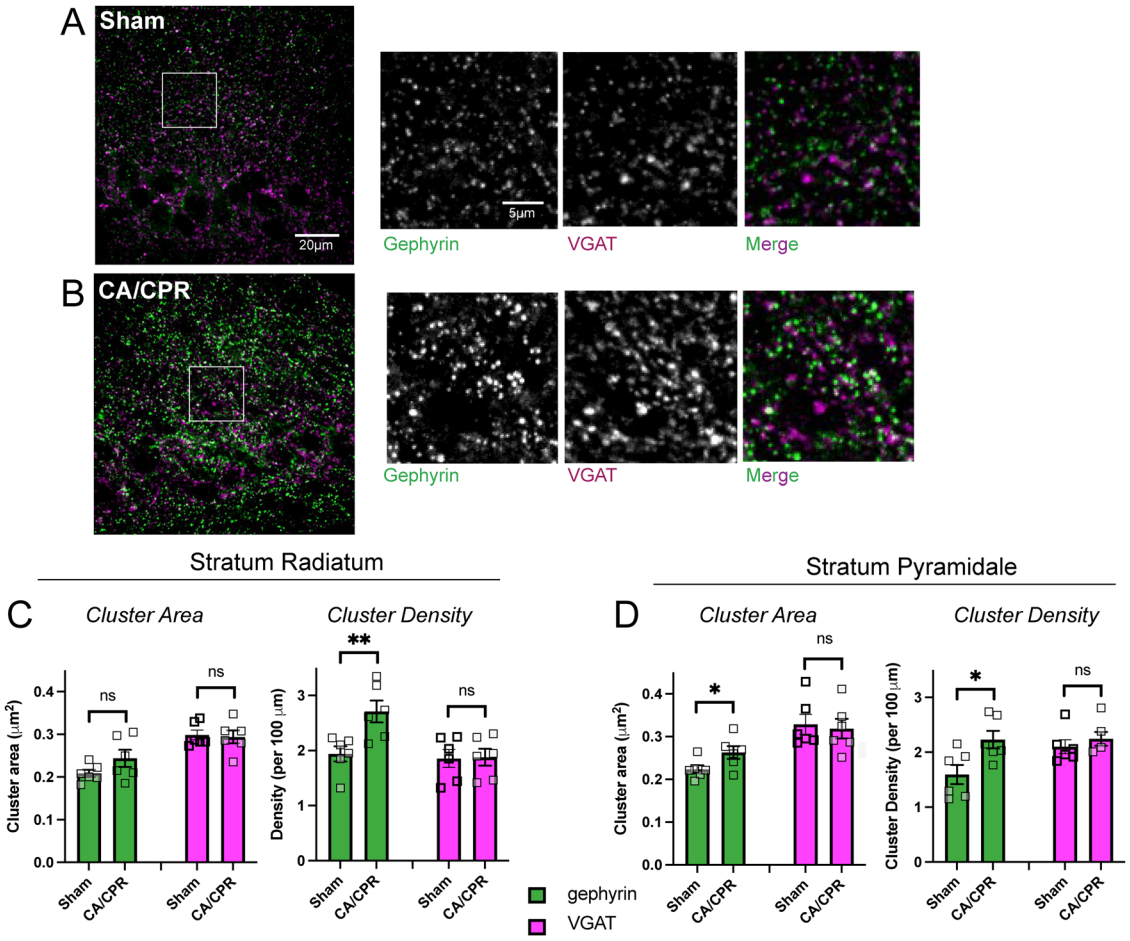

Figure 3. CA/CPR induces a persistent increase in gephyrin clustering and density. ***A***, ***B***, Shown are representative images of the CA1 region of the hippocampus from (***A***) sham-operated and (***B***) CA/CPR mice. Gephyrin staining is shown in green and VGAT is shown in magenta. ***C***, Quantification of the cluster area and density of both gephyrin and VGAT in the stratum radiatum; $n = 6$ animals per group; unpaired t test. ***D***, Quantification of the cluster area and density of both gephyrin and VGAT in the stratum pyramidale; $n = 6$ animals per group; unpaired t test. Values represent mean ± SEM. $*p < 0.05$; $**p < 0.01$.

Table 7. Statistical details for Figure 3

Statistical test	Test statistic, degrees of freedom	Post hoc test	Comparisons	*p*-value	Mean difference	95% confidence interval
Figure 3*C* —stratum radiatum cluster						
Unpaired *t* test	$t = 1.623$, df = 10	-	Area geph: sham vs CA/CPR	0.1356	0.03517	−0.01310 to 0.08344
Unpaired *t* test	$t = 0.2434$, df = 10	-	Area VGAT: sham vs CA/CPR	0.8126	−0.004681	−0.04681 to 0.03759
Unpaired *t* test	$t = 3.194$, df = 10	-	Density geph: sham vs CA/CPR	0.0096	0.7696	0.2327 to 1.307
Unpaired *t* test	$t = 0.1013$, df = 10	-	Density VGAT: sham vs CA/CPR	0.9214	0.02252	−0.4731 to 0.5182
Figure 3*D* —stratum pyramidale cluster						
Unpaired *t* test	$t = 2.249$, df = 10	-	Area geph: sham vs CA/CPR	0.0483	0.3945	0.0003631 to 0.07854
Unpaired *t* test	$t = 0.3077$, df = 10	-	Area VGAT: sham vs CA/CPR	0.7646	−0.01002	−0.08257 to 0.06253
Unpaired *t* test	$t = 2.681$, df = 10	-	Density geph: sham vs CA/CPR	0.0230	0.6363	0.1075 to 1.165
Unpaired *t* test	$t = 0.8069$, df = 10	-	Density VGAT: sham vs CA/CPR	0.4385	0.1430	−0.2519 to 0.5379

reoxygenation and treated with either tatM2NX or CTZ 1 h prior to fixation (Fig. 7*A*). We again immunostained for gephyrin, surface $GABA_AR$-γ2, and VGAT and imaged dendritic segments of pyramidal neurons (Fig. 7*B*). Treatment with tatM2NX, a potent and specific TRPM2 inhibitor, reduced the OGD-induced increase in gephyrin (Fig. 7*C*; Table 11) and surface $GABA_AR$-γ2 subunit cluster area and density (Fig. 7*D*; Table 11) as well as the presynaptic marker, VGAT (Fig. 7*E*; Table 11). We then performed similar experiments using the noncompetitive TRPM2 blocker, CTZ. We found CTZ treatment also significantly reduces the OGD effect on gephyrin (Fig. 7*F*; Table 11) and surface $GABA_AR$-γ2 (Fig. 7*G*; Table 11) cluster area and density, with a reduction in the OGD-induced increase in VGAT cluster density (Fig. 7*H*; Table 11). Using two pharmacological inhibitors of TRPM2, our data strongly support that the persistent OGD-induced increase in postsynaptic $GABA_AR$ density is TRPM2-dependent, consistent with the in vivo functional data which implicates TRPM2 activity in the increase in GABAergic sIPSC amplitude post-CA/CPR (Fig. 2).

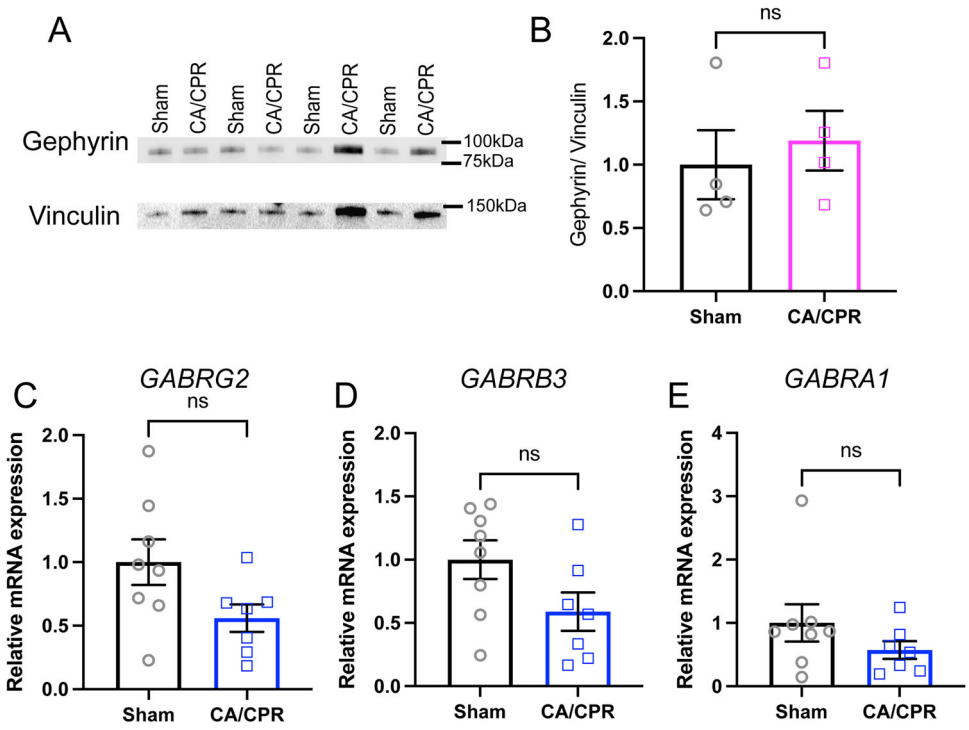

Figure 4. Protein and mRNA expression of postsynaptic GABAergic components are unaltered 7 d following CA/CPR. ***A***, Western immunoblot measuring total levels of gephyrin normalized to vinculin loading control in the P2 fraction from whole hippocampi. ***B***, Quantification of gephyrin levels normalized to mean sham; $n = 4$ animals per condition; unpaired t test. ***C–E***, Levels of mRNA transcript in CA1 hippocampal isolates as measured by quantitative qPCR for genes encoding the $GABA_AR$-γ2 (***C***), $GABA_AR$-b3 (***D***), $GABA_AR$-a1 (***E***) subunits; $n = 8$ animals per condition; unpaired t test. Values represent mean ± SEM.

Table 8. Statistical details for Figure 4

Statistical test	Test statistic, degrees of freedom	Comparisons	*p*-value	Mean difference	95% confidence interval
Figure 4*B*—gephyrin Western					
Unpaired *t* test	$t = 0.5292$, df = 6	Sham vs CA/CPR	$p = 0.6157$	0.1905	−0.6905 to 1.072
Figure 4*C*—*GABRG2*					
Unpaired *t* test	$t = 2.032$, df = 13	Sham vs CA/CPR	$p = 0.0631$	−0.4409	−0.9095 to 0.02777
Figure 4*D*—*GABRB3*					
Unpaired *t* test	$t = 1.904$, df = 13	Sham vs CA/CPR	$p = 0.0793$	−0.4104	−0.8761 to 0.05522
Figure 4*E*—*GABRA1*					
Unpaired *t* test	$t = 1.243$, df = 13	Sham vs CA/CPR	$p = 0.2340$	−0.4276	−1.171 to 0.3156

Ca^{2+} signaling and CaMKII activity contribute to CA/CPR-induced increase in GABA sIPSC amplitude

While these data implicate TRPM2 in the ischemia-induced enhancement of postsynaptic inhibitory function, the downstream signaling required to regulate $GABA_AR$ density remains yet to be determined. We hypothesized that TRPM2-mediated Ca^{2+} influx may modulate postsynaptic $GABA_AR$ function. To examine this, we performed patch-clamp recordings with a high concentration of BAPTA (10 mM), a selective Ca^{2+} buffer, in the patch pipette and recorded GABA sIPSCs from the same cell before and after CTZ treatment (Fig. 8*A*). Our results showed Ca^{2+} chelation in the postsynaptic neuron occluded the CA/CPR-induced enhancement of sIPSC mean amplitude, as there was no longer a difference between CA/CPR and sham conditions (Fig. 8B_1; Table 12). Further, we did not observe a change in amplitude following CTZ treatment in cells recorded with BAPTA in the patch pipette (Fig. 8B_1; Table 12). We also found no differences between the CA/CPR and sham conditions and the CTZ treatment in the frequency (Fig. 8B_2; Table 12) or the tau decay (Fig. 8B_3; Table 12) of sIPSCs when BAPTA was present. Given the lack of additive effect of BAPTA and CTZ on sIPSC amplitude, this suggests that postsynaptic Ca^{2+} signaling mediates the observed TRPM2-dependent increase in inhibition.

CaMKII is a Ca^{2+}-dependent kinase that has been previously shown to be required for activity-dependent postsynaptic $GABA_AR$ potentiation and clustering (Petrini et al., 2014; Chiu et al., 2018; Cook et al., 2021, 2022). We therefore hypothesized that TRPM2-mediated Ca^{2+} signaling might activate CaMKII to enhance postsynaptic GABAergic function. To test this, we used western immunoblotting to detect total protein levels of CaMKII in the membrane fractions of the whole hippocampus from CA/CPR and sham mice 7 d following the surgeries. Our data show that CaMKII levels are significantly reduced in the membrane fraction of whole hippocampi (Fig. 8*C*; Table 12). Interestingly, we observed relatively higher T286 phosphorylation of CaMKII in the synaptic membrane fraction obtained from CA/CPR mice compared with sham (Fig. 8*D*; Table 12), indicating a sustained increased synaptic CaMKII activity following GCI.

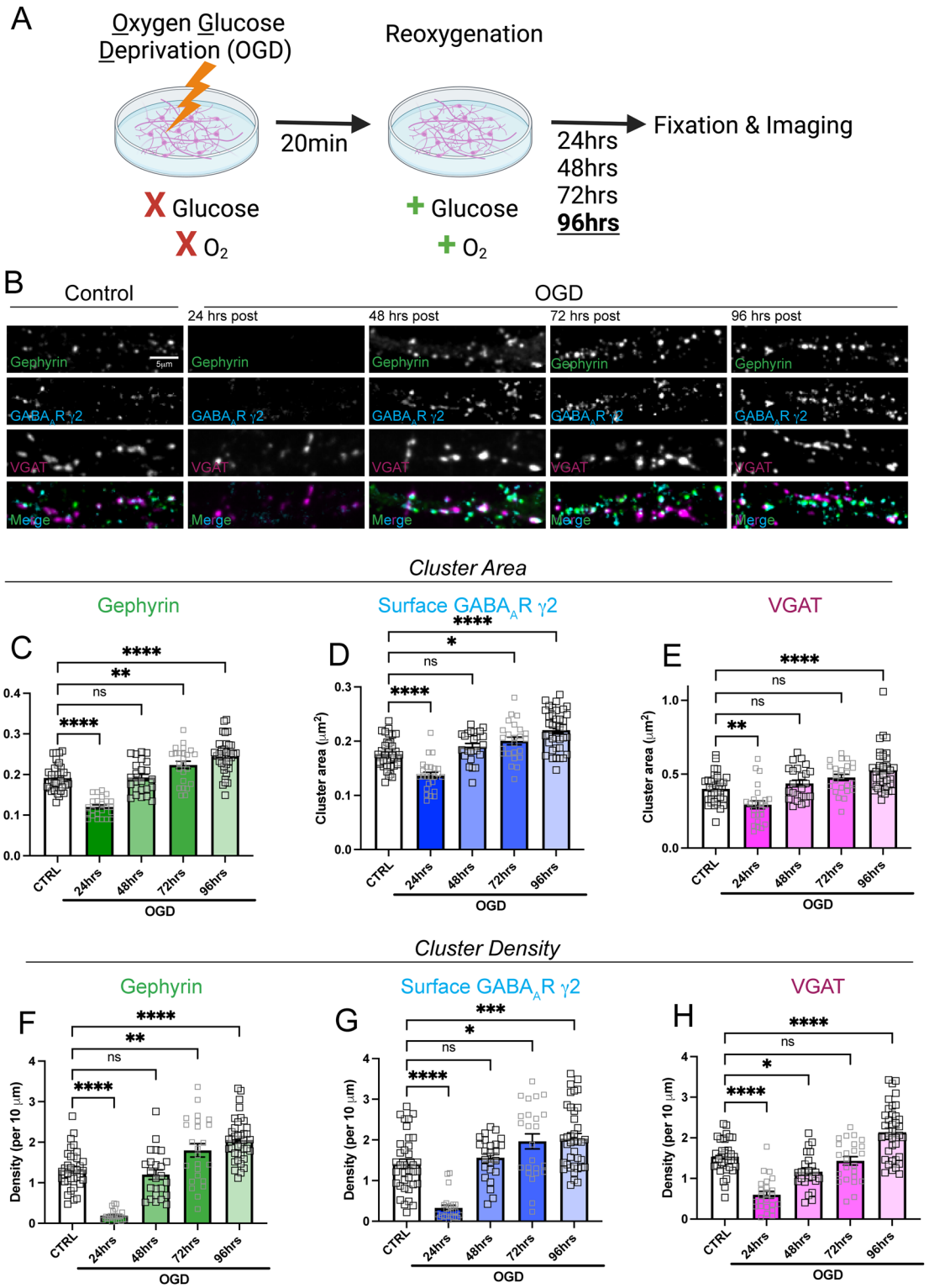

Figure 5. OGD induces a persistent increase in the clustering and density of postsynaptic GABAergic proteins. ***A***, Cartoon illustrating timeline for in vitro OGD experiments. Dissociated hippocampal neurons were reoxygenated following 20 min OGD exposure. Neurons were fixed 24, 48, 72, and 96 h following reoxygenation. ***B***, Representative confocal images of dendritic segments from pyramidal neurons stained for gephyrin (green), $GABA_AR$-γ2 subunit (cyan), and VGAT (magenta). ***C–E***, Quantification of cluster area for (***C***) gephyrin, (***D***) surface $GABA_AR$-γ2, and (***E***) VGAT; $n = 30–36$ neurons per condition; one-way ANOVA, Dunnett's post hoc. ***F–H***, Quantification of cluster density for (***F***) gephyrin, (***G***) surface $GABA_AR$-γ2, and (***H***) VGAT; $n = 30–36$ neurons per condition; one-way ANOVA, Dunnett's post hoc. Values represent mean ± SEM. $^*p < 0.05$; $^{**}p < 0.01$, $^{***}p < 0.001$, $^{****}p < 0.0001$.

To further examine the role of elevated CaMKII activity on postsynaptic GABAergic function following CA/CPR, we used patch-clamp electrophysiology to record sIPSCs while inhibiting postsynaptic CaMKII using tatCN19o (5 mM) in the patch pipette (Fig. 8*E*). Our results show that inhibition of postsynaptic CaMKII activity occluded the CA/CPR-induced increase in sIPSC amplitude, as indicated by equivalent sIPSC amplitudes observed in tatCN19o treated cells and sham conditions

Table 9. Statistical details for Figure 5

Statistical test	Test statistic, degrees of freedom	Post hoc test	Comparisons	*p*-value	Mean difference	95% confidence interval
Figure 5*C*—gephyrin cluster area						
One-way ANOVA	$F_{(4,141)} = 44.76$	Dunnett's multiple-comparisons test	CTRL-96 h vs 24 h	<0.0001	0.07153	0.04724 to 0.09581
			CTRL-96 h vs 48 h	0.9999	−0.001033	−0.02532 to 0.02325
			CTRL-96 h vs 72 h	0.0053	−0.03189	−0.05618 to −0.007609
			CTRL-96 h vs 96 h	<0.0001	−0.05309	−0.07452 to −0.03166
Figure 5*D*—$GABA_AR$-γ2 surface cluster area						
One-way ANOVA	$F_{(4,141)} = 27.68$	Dunnett's multiple-comparisons test	CTRL-96 h vs 24 h	<0.0001	0.03973	0.01888 to 0.06058
			CTRL-96 h vs 48 h	0.3002	−0.01389	−0.03474 to 0.006960
			CTRL-96 h vs 72 h	0.0169	−0.02418	−0.04503 to −0.003329
			CTRL-96 h vs 96 h	<0.0001	−0.04414	−0.06254 to −0.02573
Figure 5*E*—VGAT cluster area						
One-way ANOVA	$F_{(4,141)} = 15.80$	Dunnett's multiple-comparisons test	CTRL-96 h vs 24 h	0.0029	0.1079	0.03010 to 0.1857
			CTRL-96 h vs 48 h	0.6135	−0.03656	−0.1144 to 0.04124
			CTRL-96 h vs 72 h	0.0534	−0.07698	−0.1548 to 0.0008164
			CTRL-96 h vs 96 h	0.0029	−0.1261	−0.1948 to −0.05748
Figure 5*F* —gephyrin cluster density						
One-way ANOVA	$F_{(4,141)} = 48.24$	Dunnett's multiple-comparisons test	CTRL-96 h vs 24 h	<0.0001	1.134	0.7799 to 1.488
			CTRL-96 h vs 48 h	0.8184	0.1230	−0.2311 to 0.4772
			CTRL-96 h vs 72 h	0.0041	−0.4760	−0.8301 to −0.1218
			CTRL-96 h vs 96 h	<0.0001	−0.7311	−1.044 to −0.4186
Figure 5*G*—$GABA_AR$-γ2 surface cluster density						
One-way ANOVA	$F_{(4,141)} = 25.89$	Dunnett's multiple-comparisons test	CTRL-96 h vs 24 h	<0.0001	1.083	0.6321 to 1.535
			CTRL-96 h vs 48 h	0.8400	−0.1500	−0.6013 to 0.3013
			CTRL-96 h vs 72 h	0.0109	−0.5505	−1.002 to −0.09922
			CTRL-96 h vs 96 h	0.0007	−0.6198	−1.018 to −0.2215
Figure 5*H*—VGAT cluster density						
One-way ANOVA	$F_{(4,141)} = 37.32$	Dunnett's multiple-comparisons test	CTRL-96 h vs 24 h	<0.0001	0.9371	0.6080 to 1.266
			CTRL-96 h vs 48 h	0.0216	0.3704	0.04134 to 0.6995
			CTRL-96 h vs 72 h	0.8663	0.1029	−0.2261 to 0.4320
			CTRL-96 h vs 96 h	<0.0001	−0.6044	−0.8949 to −0.3140

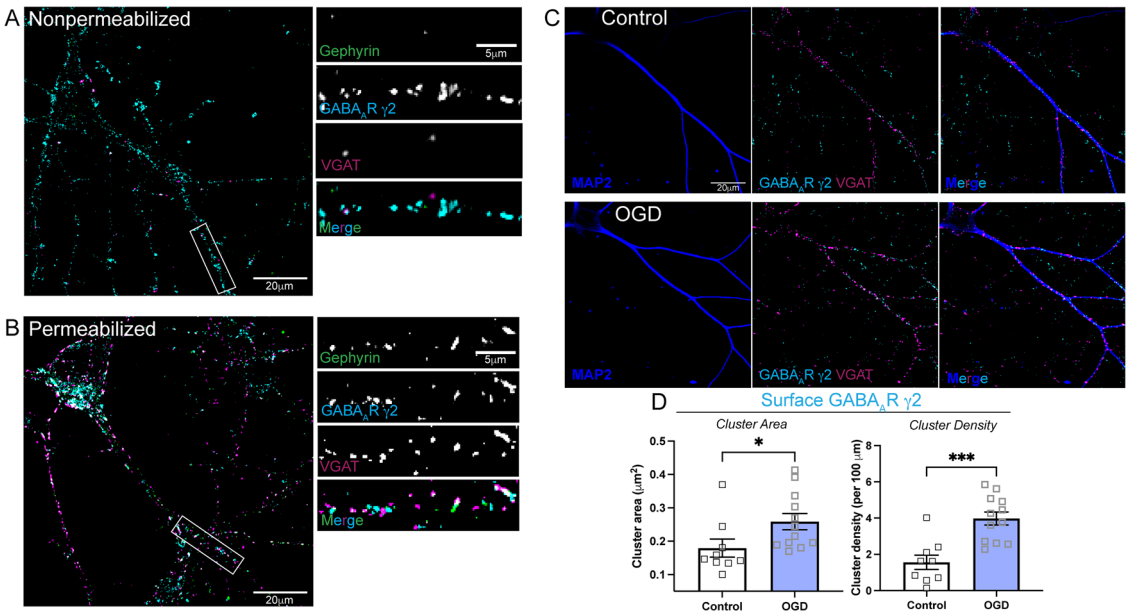

Figure 6. Validation of immunostaining in oxygen–glucose deprivation experiments. ***A***, Representative low magnification image of CA1 pyramidal neuron (left) and high magnification images of dendritic segments (right) following gephyrin (green), $GABA_AR$-γ2 subunit (cyan), and VGAT (magenta) staining under nonpermeabilizing conditions 96 h following OGD. ***B***, Representative low magnification image of CA1 pyramidal neuron (left) and high magnification images of dendritic segments (right) following gephyrin (green), $GABA_AR$-γ2 subunit (cyan), and VGAT (magenta) staining under permeabilizing conditions 96 h following OGD. ***C***, Low magnification representative images of CA1 pyramidal neurons immunostained for MAP2 (blue), $GABA_AR$-γ2 subunit (cyan), and VGAT (magenta) following control (top) and 96 h-OGD (bottom) treatment. ***D***, Subset analysis of cluster area (left) and cluster density (right) $GABA_AR$-γ2 subunit are increased 96 h following OGD using MAP2 as a guide for ROI analysis; $n = 9$–12 neurons per condition, unpaired *t* test. Values represent mean ± SEM. $*p < 0.05$; $***p < 0.001$.

Table 10. Statistical details for Figure 6

Statistical test	Test statistic, degrees of freedom	Comparisons	*p*-value	Mean difference	95% confidence interval
Figure 6*D* —cluster area					
Unpaired *t* test	$t = 2.163$, df = 19	Control vs OGD	$p = 0.0435$	0.07949	0.002566–0.1564
Figure 6*D* —cluster density					
Unpaired *t* test	$t = 4.483$, df = 19	Control vs OGD	$p = 0.0003$	2.418	1.289–3.547

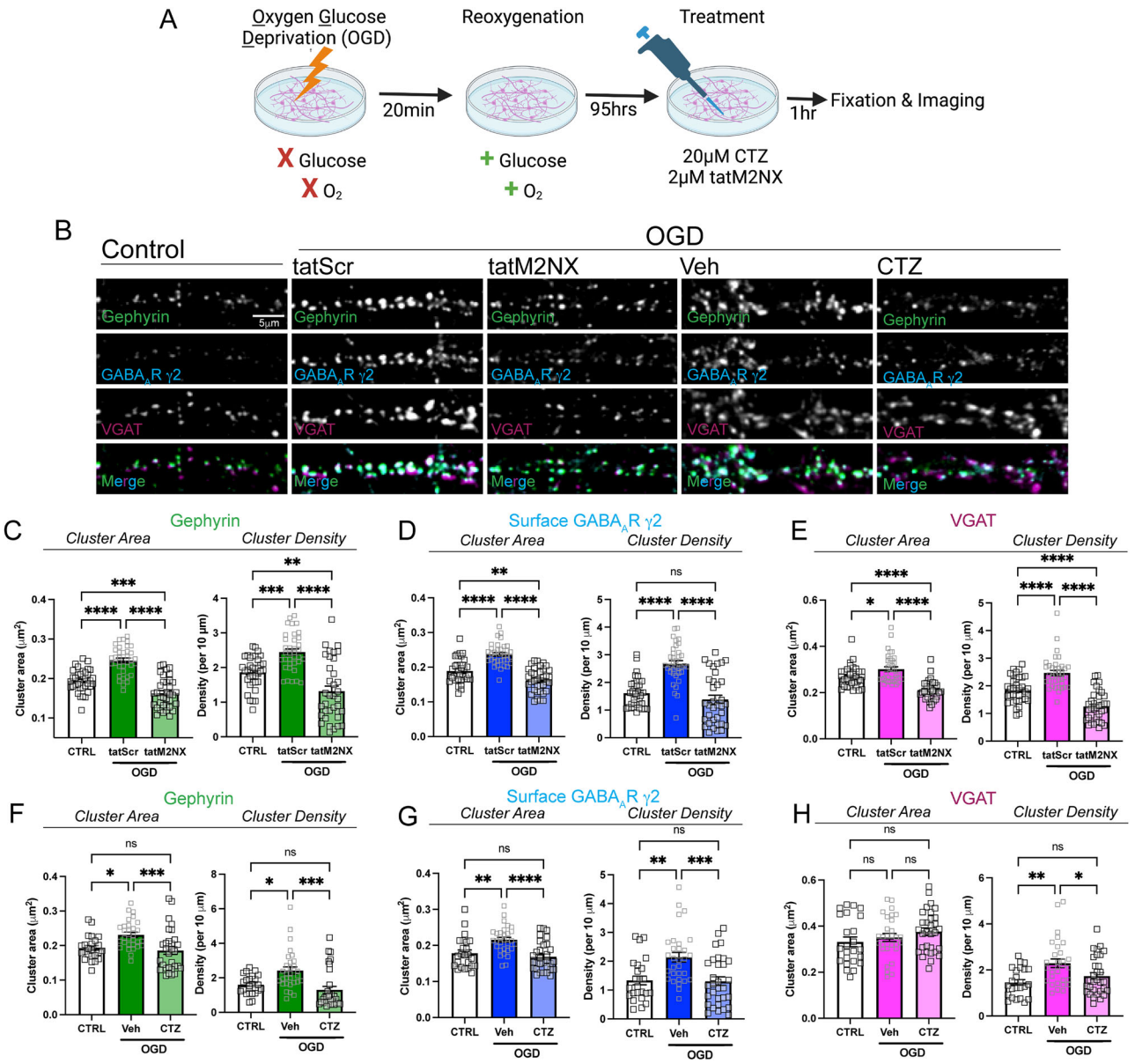

Figure 7. The TRPM2 ion channel mediates the OGD-induced increase in the clustering of postsynaptic GABAergic proteins. ***A***, Cartoon illustrating experimental timeline for neurons subjected to OGD reoxygenation and treated with tatM2NX (2 mM) or CTZ (20 mM) 1 h prior to fixation. ***B***, Representative confocal images of dendritic segments from pyramidal neurons immunostained for gephyrin (green), $GABA_AR$-γ2 subunit (cyan), and VGAT (magenta). ***C–E***, Quantification of cluster area (left) and cluster density (right) following treatment with tatM2NX for (***C***) gephyrin, (***D***) surface $GABA_AR$-γ2, and (***E***) VGAT; $n = 30–36$ neurons per condition; one-way ANOVA, Tukey's post hoc. ***F–H***, Quantification of cluster area (left) and cluster density (right) following treatment with CTZ for (***F***) gephyrin, (***G***) surface $GABA_AR$-γ2, and (***H***) VGAT, $n = 30–36$ neurons per condition; one-way ANOVA, Tukey's post hoc. Values represent mean ± SEM. $^*p < 0.05$; $^{**}p < 0.01$, $^{***}p < 0.001$, $^{****}p < 0.0001$.

(Fig. $8F_1$; Table 12). Additionally, CTZ no longer impacted the mean amplitude of sIPSCs in the CA/CPR mice recorded with tatCN19o (Fig. $8F_1$; Table 12). Similar to the effects observed with Ca^{2+} chelation, we did not observe a change between the CA/CPR and sham conditions and the CTZ treatment in the frequency (Fig. $8F_2$; Table 12) and tau decay (Fig. $8F_3$; Table 12) of sIPSCs when the CaMKII inhibitor was present. These results indicate that CaMKII-dependent increases in postsynaptic inhibitory function could be downstream of Ca^{2+} entry via TRPM2 channel activity.

Table 11. Statistical details for Figure 7

Statistical test	Test statistic, degrees of freedom	Post hoc test	Comparisons	*p*-value	Mean difference	95% confidence interval
Figure 7C —gephyrin cluster area tatM2NX						
One-way ANOVA	$F_{(2,104)} = 53.15$	Tukey's multiple-comparisons test	CTRL vs tatScr	<0.0001	−0.05139	−0.07079 to −0.03199
			CTRL vs tatM2NX	0.0006	0.03135	0.01195 to 0.05075
			tatScr vs tatM2NX	<0.0001	0.08274	0.06348 to 0.1020
Figure 7C —gephyrin cluster density tatM2NX						
One-way ANOVA	$F_{(2,105)} = 27.36$	Tukey's multiple-comparisons test	CTRL vs tatScr	0.0007	−0.5814	−0.9437 to −0.2191
			CTRL vs tatM2NX	0.0015	0.5456	0.1833 to 0.9079
			tatScr vs tatM2NX	<0.0001	1.127	0.7647 to 1.489
Figure 7D—surface $GABA_AR$-γ2 cluster area tatM2NX						
One-way ANOVA	$F_{(2,104)} = 44.98$	Tukey's multiple-comparisons test	CTRL vs tatScr	<0.0001	−0.04776	−0.06656 to −0.02896
			CTRL vs tatM2NX	0.0036	0.02621	0.007408 to 0.04501
			tatScr vs tatM2NX	<0.0001	0.07397	0.05517 to 0.09276
Figure 7D—surface $GABA_AR$-γ2 cluster density tatM2NX						
One-way ANOVA	$F_{(2,105)} = 33.02$	Tukey's multiple-comparisons test	CTRL vs tatScr	<0.0001	−1.065	−1.468 to −0.6621
			CTRL vs tatM2NX	0.3884	0.2233	−0.1794 to 0.6260
			tatScr vs tatM2NX	<0.0001	1.288	0.8853 to 1.691
Figure 7E—VGAT cluster area tatM2NX						
One-way ANOVA	$F_{(2,105)} = 31.10$	Tukey's multiple-comparisons test	CTRL vs tatScr	0.0139	−0.03322	−0.06080 to −0.005640
			CTRL vs tatM2NX	<0.0001	0.05722	0.02964 to 0.08480
			tatScr vs tatM2NX	<0.0001	0.09044	0.06286 to 0.1180
Figure 7E—VGAT cluster density tatM2NX						
One-way ANOVA	$F_{(2,105)} = 46.17$	Tukey's multiple-comparisons test	CTRL vs tatScr	<0.0001	−0.6126	−0.9120 to −0.3132
			CTRL vs tatM2NX	<0.0001	0.5976	0.2982 to 0.8970
			tatScr vs tatM2NX	<0.0001	1.210	0.9108 to 1.510
Figure 7F—gephyrin cluster area CTZ						
One-way ANOVA	$F_{(2,82)} = 7.994$	Tukey's multiple-comparisons test	CTRL vs Veh	0.0107	−0.03851	−0.06944 to −0.007576
			CTRL vs CTZ	0.8445	0.007133	−0.02358 to 0.03784
			Veh vs CTZ	0.0009	0.04564	0.01671 to 0.07457
Figure 7F—gephyrin cluster density CTZ						
One-way ANOVA	$F_{(2,82)} = 9.922$	Tukey's multiple-comparisons test	CTRL vs Veh	0.0109	−0.8179	−1.476 to −0.1597
			CTRL vs CTZ	0.5200	0.2997	−0.3538 to 0.9532
			Veh vs CTZ	0.0001	1.118	0.5021 to 1.733
Figure 7G—surface $GABA_AR$-γ2 cluster area CTZ						
One-way ANOVA	$F_{(2,82)} = 11.17$	Tukey's multiple-comparisons test	CTRL vs Veh	0.0034	−0.03717	−0.06362 to −0.01071
			CTRL vs CTZ	0.6531	0.009704	−0.01656 to 0.03596
			Veh vs CTZ	<0.0001	0.04687	0.02213 to 0.07161
Figure 7G—surface $GABA_AR$-γ2 cluster density CTZ						
One-way ANOVA	$F_{(2,82)}$=	Tukey's multiple-comparisons test	CTRL vs Veh	0.0025	−0.8037	−1.359 to −0.2482
			CTRL vs CTZ	0.9916	0.02858	−0.5230 to 0.5801
			Veh vs CTZ	0.0007	0.8323	0.3128 to 1.352
Figure 7H—VGAT cluster area CTZ						
One-way ANOVA	$F_{(2,82)} = 1.455$	Tukey's multiple-comparisons test	CTRL vs Veh	0.7481	−0.01898	−0.08130 to 0.04334
			CTRL vs CTZ	0.2163	−0.04339	−0.1048 to 0.01802
			Veh vs CTZ	0.5799	−0.02440	−0.08275 to 0.03394
Figure 7H—VGAT cluster density CTZ						
One-way ANOVA	$F_{(2,82)}$=	Tukey's multiple-comparisons test	CTRL vs Veh	0.0015	−0.8347	−1.388 to −0.2818
			CTRL vs CTZ	0.4455	−0.2803	−0.8292 to 0.2686
			Veh vs CTZ	0.0327	0.5544	0.03734 to 1.071

Ca^{2+}-dependent CaMKII activity contributes to increased clustering of postsynaptic GABAergic components via a TRPM2-dependent pathway

We next investigated whether TRPM2- and CaMKII-mediated enhancement of postsynaptic sIPSC amplitude was due to an increase in the density of postsynaptic $GABA_ARs$. To assess this, we used the 96 h timepoint following OGD reoxygenation in dissociated rat hippocampal neurons and treated cells with vehicle (control), tatCN19o alone, or combined tatCN19o and tatM2NX 1 h prior to fixation (Fig. 9*A*) and immunostained for GABAergic synaptic markers (Fig. 9*B*). We found that treatment with tatCN19o reduced the cluster area and density of the $GABA_AR$-γ2 (Fig. 9*D*; Table 13) and gephyrin (Fig. 9*C*; Table 13) following OGD compared with the OGD vehicle control. Additionally, we observed a significant decrease in the cluster area and density of the postsynaptic components in the combined tatM2NX and tatCN19o condition compared with the control (veh) condition following OGD; however, there was no additional reduction in the cluster area and density of the postsynaptic inhibitory synaptic proteins in the combined treatment condition compared with the tatCN19o alone (Fig. 9*C,D*; Table 13). We found no differences across all conditions when measuring the VGAT cluster area, but we did observe a decrease in VGAT cluster density in the combined condition (Fig. 9*E*; Table 13). These results suggest that TRPM2 and CaMKII likely converge on the same pathway to regulate postsynaptic $GABA_AR$ density.

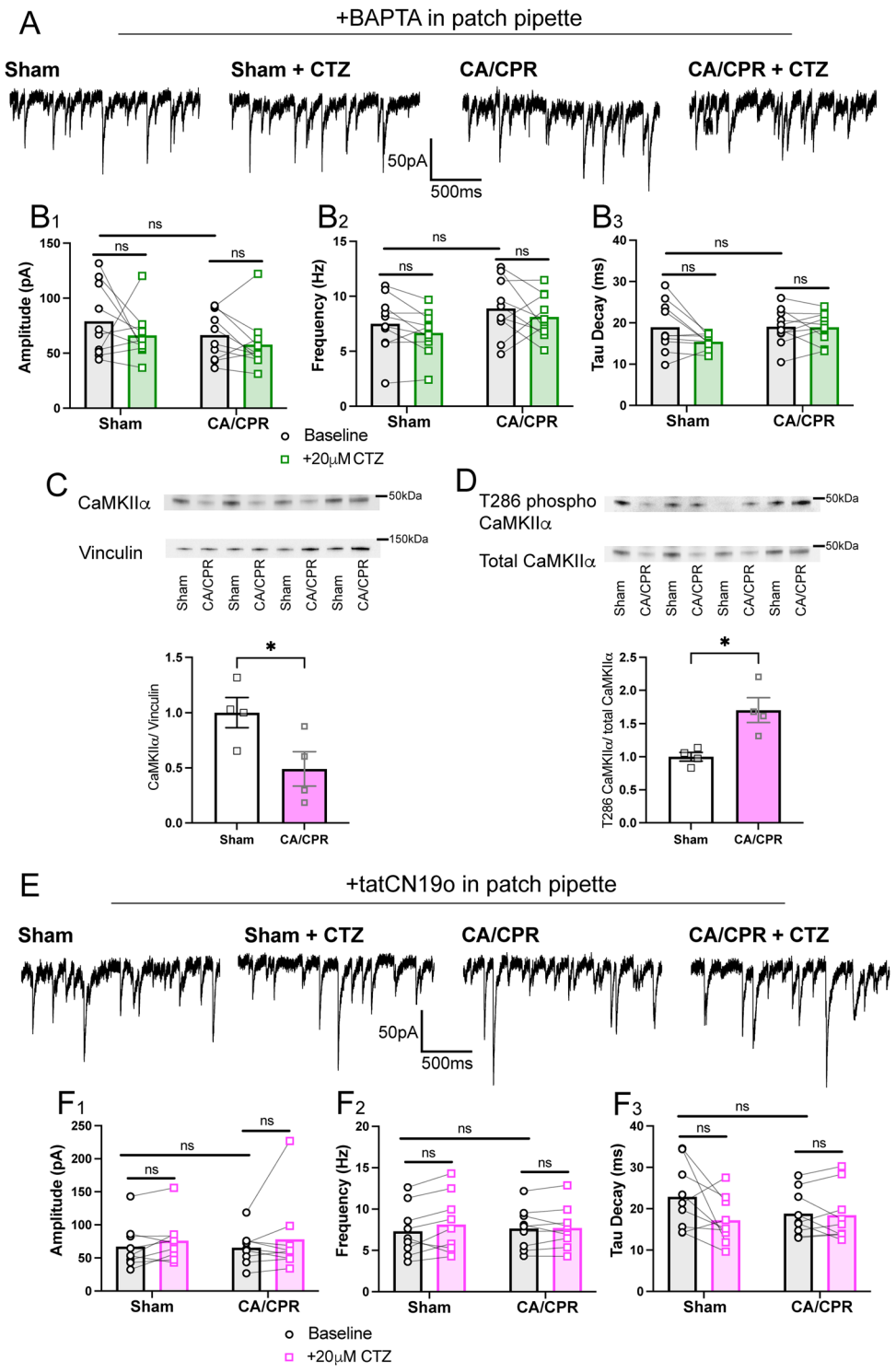

Figure 8. Ca^{2+} signaling and CaMKII activity contribute to CA/CPR-induced increase in the amplitude of GABA sIPSCs. ***A***, Representative traces from sham (far left), sham after CTZ from the same cell (center left), CA/CPR (center right), and CA/CPR after CTZ from the same cell (far right). BAPTA (10 mM) was included in the patch pipette across all conditions. ***B***, Mean amplitude (1), frequency (2), and tau decay (3) kinetics were measured from sIPSC events in the same cell before and after bath application of CTZ from sham and CA/CPR operated mice with 10 mM BAPTA included in patch pipette; $n = 10$ cells/4–7 animals per condition; two-way ANOVA with repeated measures, Sidak's post hoc test. ***C***, Western immunoblot measuring total levels of CaMKII normalized to vinculin loading control in the membrane fraction of whole hippocampi from sham and CA/CPR operated mice; $n = 5$ animals per condition; unpaired *t* test. ***D***, Western immunoblot measuring levels of T286 phosphorylation of CaMKII normalized to total CaMKII in the membrane fraction of whole hippocampi from sham and CA/CPR operated mice; $n = 4$ animals per condition; unpaired *t* test. ***E***, Representative traces from sham (far left), sham after CTZ from the same cell (center left), CA/CPR (center right), and CA/CPR after CTZ from the same cell (far right). TatCN19o (5 mM) was included in the patch pipette across all conditions. ***F***, Mean amplitude (1), frequency (2), and tau decay (3) kinetics were measured from sIPSC events in the same cell before and after bath application of CTZ from sham and CA/CPR operated mice with 5 mM tatCN19o included in patch pipette; $n = 9$ cells/45 animals per condition; two-way ANOVA with repeated measures, Sidak's post hoc test. Values represent mean ± SEM. $^*p < 0.05$.

Table 12. Statistical details for Figure 8

Statistical test	Test statistic, degrees of freedom, *p*-value (of interaction if two-way)	Post hoc test	Comparisons	*p*-value	Mean difference	95% confidence interval
Figure 8B_1—BAPTA amplitude						
Two-way ANOVA	$F_{(1,18)} = 0.08304$, $p = 0.7765$	Sidak's multiple comparisons	Sham – CA/CPR Baseline	0.4878	12.53	−14.37 to 39.44
			Sham – CA/CPR Post-CTZ	0.7264	8.286	−18.62 to 35.19
			Baseline – post-CTZ Sham	0.4134	12.82	−12.58 to 38.22
			Baseline – post-CTZ CA/CPR	0.6646	8.579	−16.82 to 33.98
Figure 8B_2—BAPTA frequency						
Two-way ANOVA	$F_{(1,18)} = 0.004294$, $p = 0.9485$	Sidak's multiple comparisons	Sham – CA/CPR Baseline	0.3469	−1.391	−3.830 to 1.049
			Sham – CA/CPR Post-CTZ	0.3155	−1.454	−3.894 to 0.9850
			Baseline – post-CTZ Sham	0.4283	0.8306	−0.8507 to 2.512
			Baseline – post-CTZ CA/CPR	0.4826	0.7667	−0.9146 to 2.448
Figure 8B_3—BAPTA tau decay						
Two-way ANOVA	$F_{(1,18)} = 2.824$, $p = 0.1101$	Sidak's multiple comparisons	Sham – CA/CPR Baseline	0.9969	−0.1335	−4.583 to 4.316
			Sham – CA/CPR Post-CTZ	0.1470	−3.479	−7.929 to 0.9713
			Baseline – post-CTZ Sham	0.0459	3.492	0.05949 to 6.925
			Baseline – post-CTZ CA/CPR	0.9933	0.1472	−3.286 to 3.580
Figure 8*C*—CaMKII Western						
Unpaired *t* test	$t = 2.459$, df = 6	-	Sham vs CA/CPR	0.0116	0.7037	0.2227 to 1.185
Figure 8*D*—T286 PhosphoCaMKII Western						
Unpaired *t* test	$t = 3.580$, df = 6	-	Sham vs CA/CPR	0.0492	−0.5095	−1.017 to −0.002418
Figure 8F_1—tatCN19o amplitude						
Two-way ANOVA	$F_{(1,16)} = 0.08021$, $p = 0.7806$	Sidak's multiple comparisons	Sham – CA/CPR Baseline	0.9947	1.730	−42.25 to 45.71
			Sham – CA/CPR Post-CTZ	0.9920	−2.125	−46.11 to 41.86
			Baseline – post-CTZ Sham	0.6109	−8.762	−32.51 to 14.98
			Baseline – post-CTZ CA/CPR	0.3734	−12.62	−36.36 to 11.13
Figure 8F_2—tatCN19o frequency						
Two-way ANOVA	$F_{(1,16)} = 2.247$, $p = 0.1533$	Sidak's multiple comparisons	Sham – CA/CPR Baseline	0.9638	−0.3370	−3.595 to 2.921
			Sham – CA/CPR Post-CTZ	0.9462	0.4130	−2.845 to 3.671
			Baseline – post-CTZ Sham	0.0681	−0.8167	−1.689 to 0.05588
			Baseline – post-CTZ CA/CPR	0.9784	−0.06667	−0.9392 to 0.8059
Figure 8F_3—tatCN19o tau ecay						
Two-way ANOVA	$F_{(1,16)} = 2.973$	Sidak's multiple comparisons	Sham – CA/CPR Baseline	0.0381	5.661	0.2960 to 11.03
			Sham – CA/CPR Post-CTZ	0.9836	0.3568	−5.009 to 5.722
			Baseline – post-CTZ Sham	0.3510	4.080	−3.141 to 11.30
			Baseline – post-CTZ CA/CPR	0.9059	−1.225	−8.446 to 5.996

The tatCN19o peptide was shown to block both the Ca^{2+}-independent autonomous and Ca^{2+}-stimulated CaMKII activity (Vest et al., 2010). Based on our functional data showing that Ca^{2+} signaling was required for the increase in sIPSC amplitude and is reversible with Ca^{2+} chelation (Fig. 9), we hypothesized that the Ca^{2+}-stimulated CaMKII activity contributes to elevated $GABA_AR$ clustering. To test this, we treated neurons 96 h following OGD reoxygenation with KN93 (5 mM), a small molecule CaMKII inhibitor known to preferentially block Ca^{2+}-stimulated CaMKII activity (Fig. 9*A*; Vest et al., 2010).

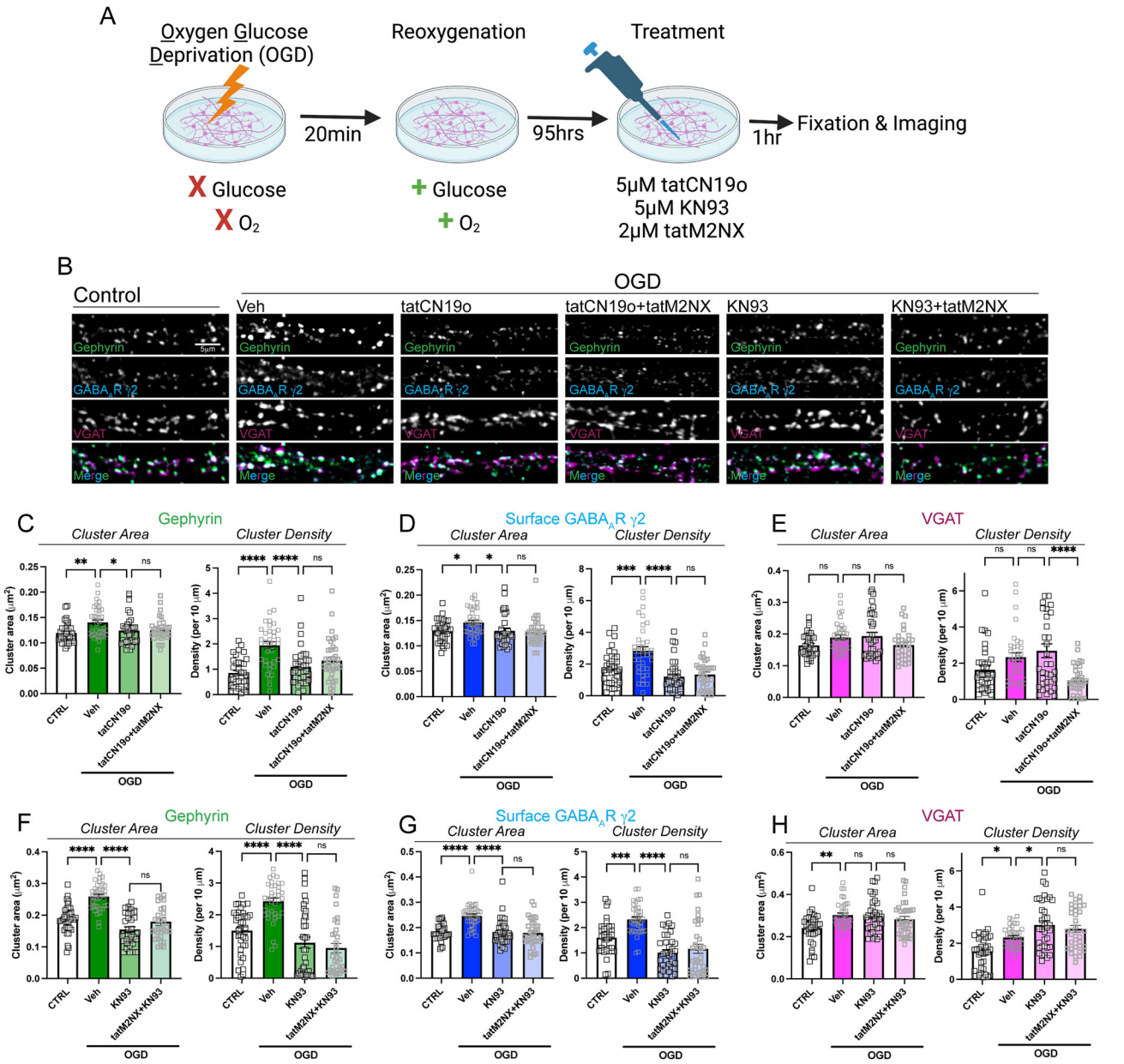

Figure 9. Ca^{2+}-dependent CaMKII activity contributes to the increased clustering of postsynaptic GABAergic proteins via a TRPM2-dependent pathway. ***A***, Cartoon illustrating experimental timeline for neurons subjected to OGD reoxygenation and treated with tatCN19o (5 mM), KN93 (5 mM), or combined treatment with tatM2NX (2 mM) 1 h prior to fixation. ***B***, Representative confocal images of dendritic segments from pyramidal neurons stained for gephyrin (green), $GABA_AR$-γ2 subunit (cyan), and VGAT (magenta). ***C–E***, Quantification of cluster area (left) and density (right) following treatment with tatCN19o or tatCN19o + tatM2NX for (***C***) gephyrin, (***D***) surface $GABA_AR$-γ2, and (***E***) VGAT; $n = 30–36$ neurons per condition; one-way ANOVA, Tukey's post hoc. ***F–H***, Quantification of cluster area (left) and density (right) following treatment with KN93 or KN93 + tatM2NX for (***E***) gephyrin, (***F***) surface $GABA_AR$-γ2, and (***G***) VGAT; $n = 30–36$ neurons per condition; one-way ANOVA, Tukey's post hoc. Values represent mean ± SEM. $*p < 0.05$; $**p < 0.01$; $***p < 0.001$; $****p < 0.0001$.

We found that KN93 significantly reduced the cluster area and density of both postsynaptic GABAergic proteins following OGD compared with the OGD vehicle control condition (Fig. 9*F,G*; Table 13). This reduction in cluster area of postsynaptic components persisted in the combined KN93 and tatM2NX condition, showing no differences compared with KN93 treatment alone following OGD (Fig. 9*F,G*; Table 13). While there was a significant increase in the presynaptic marker, VGAT, cluster area, and density in the vehicle OGD condition compared with the control no OGD group, neither KN93 nor the combined KN93 and tatM2NX treatment reduced the VGAT cluster size and density (Fig. 9*H*; Table 13). Altogether, these data suggest that the TRPM2 channel and Ca^{2+}-stimulated CaMKII activity converge on the same molecular pathway to regulate postsynaptic $GABA_A$ receptor density at delayed timepoints following OGD.

Discussion

Here, we combine in vitro and in vivo approaches to elucidate the enhancement of postsynaptic GABAergic function in the hippocampus, accounting for the reduction in the E/I ratio and driving the LTP deficits following CA/CPR. Using an in vitro model that emulates the direct ischemic insult to the hippocampus observed in GCI, we found a shift from an acute reduction in GABAergic signaling to a sustained elevation in the clustering of GABAergic

Table 13. Statistical details for Figure 9

Statistical test	Test statistic, degrees of freedom	Post hoc test	Comparisons	*p*-value	Mean difference	95% confidence interval
Figure 9*C*—gephyrin cluster area tatCN19o						
One-way ANOVA	$F_{(3,137)} = 4.425$	Tukey's multiple comparisons	CTRL vs Veh	0.0045	−0.02070	−0.03642 to −0.004981
			CTRL vs tatCN19o	0.8733	−0.004612	−0.02044 to 0.01122
			CTRL vs tatCN19o + tatM2NX	0.7700	−0.005870	−0.02170 to 0.009963
			Veh vs tatCN19o	0.0427	0.01609	0.0003688 to 0.03181
			Veh vs tatCN19o + tatM2NX	0.0720	0.01483	−0.0008887 to 0.03056
			tatCN19o vs tatCN19o + tatM2NX	0.9969	−0.001258	−0.01709 to 0.01457
Figure 9*C*—gephyrin cluster density tatCN19o						
One-way ANOVA	$F_{(3,138)} = 12.51$	Tukey's multiple comparisons	CTRL vs Veh	<0.0001	−1.090	−1.577 to −0.6033
			CTRL vs tatCN19o	0.5600	−0.2464	−0.7367 to 0.2439
			CTRL vs tatCN19o + tatM2NX	0.0462	−0.4926	−0.9795 to −0.005706
			Veh vs tatCN19o	<0.0001	0.8438	0.3569 to 1.331
			Veh vs tatCN19o + tatM2NX	0.0087	0.5976	0.1142 to 1.081
			tatCN19o vs tatCN19o + tatM2NX	0.5551	−0.2462	−0.7331 to 0.2407
Figure 9*D*—$GABA_AR$-γ2 cluster area tatCN19o						
One-way ANOVA	$F_{(3,135)} = 7.338$	Tukey's multiple comparisons	CTRL vs Veh	0.0097	−0.01712	−0.03112 to −0.003130
			CTRL vs tatCN19o	0.8717	0.004222	−0.01020 to 0.01865
			CTRL vs tatCN19o + tatM2NX	0.7643	0.005279	−0.008816 to 0.01937
			Veh vs tatCN19o	0.0010	0.02135	0.006921 to 0.03577
			Veh vs tatCN19o + tatM2NX	0.0004	0.02240	0.008309 to 0.03650
			tatCN19o vs tatCN19o + tatM2NX	0.9976	0.001057	−0.01347 to 0.01558
Figure 9*D*—$GABA_AR$-γ2 cluster density tatCN19o						
One-way ANOVA	$F_{(3,139)} = 14.16$	Tukey's multiple comparisons	CTRL vs Veh	0.0006	−1.100	−1.817 to −0.3837
			CTRL vs tatCN19o	0.2435	0.5204	−0.2013 to 1.242
			CTRL vs tatCN19o + tatM2NX	0.4977	0.3875	−0.3291 to 1.104
			Veh vs tatCN19o	<0.0001	1.621	0.8990 to 2.342
			Veh vs tatCN19o + tatM2NX	<0.0001	1.488	0.7712 to 2.204
			tatCN19o vs tatCN19o + tatM2NX	0.9636	−0.1329	−0.8546 to 0.5888
Figure 9*E*—VGAT cluster area tatCN19o						
One-way ANOVA	$F_{(3,134)} = 4.230$	Tukey's multiple comparisons	CTRL vs Veh	0.1843	−0.02478	−0.05663 to 0.007069
			CTRL vs tatCN19o	0.0870	−0.02928	−0.06136 to 0.002800
			CTRL vs tatCN19o + tatM2NX	0.9998	−0.001075	−0.03419 to 0.03204
			Veh vs tatCN19o	0.9834	−0.004496	−0.03657 to 0.02758
			Veh vs tatCN19o + tatM2NX	0.2491	0.02371	−0.009404 to 0.05682
			tatCN19o vs tatCN19o + tatM2NX	0.1281	0.02820	−0.005126 to 0.06153
Figure 9*E*—VGAT cluster density tatCN19o						
One-way ANOVA	$F_{(3,134)}$=	Tukey's multiple comparisons	CTRL vs Veh	0.2171	−0.6884	−1.612 to 0.2354
			CTRL vs tatCN19o	0.0211	−1.045	−1.975 to −0.1143
			CTRL vs tatCN19o + tatM2NX	0.3497	0.5892	−0.3346 to 1.513
			Veh vs tatCN19o	0.7521	−0.3563	−1.287 to 0.5742
			Veh vs tatCN19o+ tatM2NX	0.0025	1.278	0.3538 to 2.201
			tatCN19o vs tatCN19o + tatM2NX	<0.0001	1.634	0.7035 to 2.564
Figure 9*F*—gephyrin cluster area KN93						
One-way ANOVA	$F_{(3,136)} = 26.50$	Tukey's multiple comparisons	CTRL vs Veh	<0.0001	−0.07101	−0.1028 to −0.03922
			CTRL vs KN93	0.0383	0.03327	0.001257 to 0.06529
			CTRL vs tatM2NX + KN93	0.9059	0.008451	−0.02405 to 0.04096
			Veh vs KN93	<0.0001	0.1043	0.07227 to 0.1363
			Veh vs tatM2NX + KN93	<0.0001	0.07946	0.04696 to 0.1120
			KN93 vs tatM2NX + KN93	0.2034	−0.02482	−0.05755 to 0.007904
Figure 9*F*—ephyrin cluster density KN93						
One-way ANOVA	$F_{(3,135)} = 22.68$	Tukey's multiple comparisons	CTRL vs Veh	<0.0001	−0.9251	−1.427 to −0.4234
			CTRL vs KN93	0.2113	0.3792	−0.1260 to 0.8845
			CTRL vs tatM2NX + KN93	0.0314	0.5521	0.03498 to 1.069
			Veh vs KN93	<0.0001	1.304	0.7991 to 1.810
			Veh vs tatM2NX + KN93	<0.0001	1.477	0.9601 to 1.994
			KN93 vs tatM2NX + KN93	0.8235	0.1728	−0.3477 to 0.6934
Figure 9*G*—$GABA_AR$-γ2 cluster area KN93						
One-way ANOVA	$F_{(3,138)} = 16.77$	Tukey's multiple comparisons	CTRL vs Veh	<0.0001	−0.06180	−0.09046 to −0.03315
			CTRL vs KN93	0.9997	0.001011	−0.02785 to 0.02987
			CTRL vs tatM2NX + KN93	0.9679	0.005088	−0.02377 to 0.03395
			Veh vs KN93	<0.0001	0.06281	0.03395 to 0.09168
			Veh vs tatM2NX + KN93	<0.0001	0.06689	0.03803 to 0.09575
			KN93 vs tatM2NX + KN93	0.9833	0.004077	−0.02499 to 0.03314

(*Table continues.*)

Table 13. Continued

Statistical test	Test statistic, degrees of freedom	Post hoc test	Comparisons	*p*-value	Mean difference	95% confidence interval
Figure 9*G*—$GABA_AR$-γ2 cluster density KN93						
One-way ANOVA	$F_{(3,138)} = 20.31$	Tukey's multiple comparisons	CTRL vs Veh	0.0008	−0.7207	−1.199 to −0.2421
			CTRL vs KN93	0.0089	0.5945	0.1125 to 1.076
			CTRL vs tatM2NX + KN93	0.0856	0.4413	−0.04072 to 0.9233
			Veh vs KN93	<0.0001	1.315	0.8332 to 1.797
			Veh vs tatM2NX + KN93	<0.0001	1.162	0.6800 to 1.644
			KN93 vs tatM2NX + KN93	0.8446	−0.1532	−0.6386 to 0.3322
Figure 9*H*—VGAT cluster area KN93						
One-way ANOVA	$F_{(3,139)} = 5.169$	Tukey's multiple comparisons	CTRL vs Veh	0.0033	−0.06090	−0.1060 to −0.01583
			CTRL vs KN93	0.0068	−0.05708	−0.1021 to −0.01202
			CTRL vs tatM2NX + KN93	0.0936	−0.04088	−0.08627 to 0.004508
			Veh vs KN93	0.9962	0.003816	−0.04125 to 0.04888
			Veh vs tatM2NX + KN93	0.6611	0.02002	−0.02537 to 0.06541
			KN93 vs tatM2NX + KN93	0.7897	0.01620	−0.02918 to 0.06159
Figure 9*H*—VGAT cluster density KN93						
One-way ANOVA	$F_{(3,139)} = 13.43$	Tukey's multiple comparisons	CTRL vs Veh	0.0128	−0.7708	−1.420 to −0.1218
			CTRL vs KN93	<0.0001	−1.462	−2.111 to −0.8125
			CTRL vs tatM2NX + KN93	<0.0001	−1.247	−1.901 to −0.5937
			Veh vs KN93	0.0322	−0.6907	−1.340 to −0.04171
			Veh vs tatM2NX + KN93	0.2346	−0.4765	−1.130 to 0.1771
			KN93 vs tatM2NX + KN93	0.8293	0.2142	−0.4394 to 0.8678

proteins at synaptic sites following OGD reoxygenation. To our knowledge, this is the first study to employ the OGD in vitro system to examine synaptic alterations days after ischemic insult following the completion of cell death processes. Using this novel in vitro paradigm and a murine model of GCI, we identified the TRPM2 ion channel as a potential mediator of E/I imbalance and GABAergic synaptic enhancement. TRPM2 inhibition effectively blocked the CA/CPR-induced increase in GABA:AMPA ratio and sIPSC amplitude and the OGD-induced effect on cluster area of postsynaptic GABAergic components. Furthermore, our data revealed that TRPM2 and Ca^{2+}-CaMKII are both required for the elevated postsynaptic GABAergic function. Chelation of Ca^{2+} and CaMKII blockade both alleviated the CA/CPR effect on sIPSC amplitude and reversed the OGD-induced increase in cluster area of synaptic GABAergic proteins. Additionally, blockade of the TRPM2 channel showed no additive effect on the reduction in sIPSC amplitude or $GABA_AR$ clustering following CaMKII inhibition, suggesting that TRPM2 and CaMKII reside in the same pathway to regulate inhibitory synaptic function after ischemia.

The elevation of excitatory signaling with concurrent loss of GABAergic inhibitory synapses in the acute period is well-defined (Alicke and Schwartz-Bloom, 1995; Schwartz-Bloom and Sah, 2001; Mele et al., 2014). E/I balance and the role of GABAergic signaling beyond acute cell death has received relatively less attention; however, emerging work provides evidence of reduced E/I balance in the surviving network, primarily driven by enhanced inhibition through extrasynaptic (tonic) $GABA_ARs$ (Carmichael, 2012; Joy and Carmichael, 2021). Excessive tonic inhibition has been demonstrated to hinder cortical and hippocampal recovery in animal models of focal ischemia (Clarkson et al., 2010; Lake et al., 2015; Orfila et al., 2019). Additionally, one study has shown phasic inhibition, achieved through rapid activation of synaptic $GABA_ARs$, is enhanced in the peri-infarct cortex following stroke, correlating with motor deficits (Hiu et al., 2016). In line with these findings, our study contributes to the existing literature by describing elevated postsynaptic phasic inhibition in the hippocampus following global insult and its potential role in impairing excitatory LTP. The question of whether excessive tonic inhibition also contributes to hippocampal synaptic plasticity deficits following GCI warrants further investigation. Altogether, our observation of elevated postsynaptic (phasic) GABAergic signaling, which can be pharmacologically interrupted/targeted without the unfavorable adverse effects of directly blocking $GABA_AR$, offers a promising approach for therapeutic development.

In our study, we identify the TRPM2 ion channel as a novel mediator of inhibitory function and E/I balance following ischemia. Although TRPM2 has been extensively studied in the context of neuronal cell death, with acute inhibition of the channel conferring neuroprotection (Jia et al., 2011; Nakayama et al., 2013; Shimizu et al., 2013), recent evidence has highlighted its involvement in the postacute phase, indicating a role for the channel in mechanisms in the expression of synaptic plasticity and its promise as a neurorestorative therapeutic target (Xie et al., 2011; Dietz et al., 2020, 2021). Our prior study revealed that sustained TRPM2 activity following GCI has been found to contribute to ischemia-induced LTP impairment via a calcineurin-GSK3b-dependent pathway within glutamatergic synapses (Dietz et al., 2020). In contrast, our data obtained here is the first to suggest an additional role for TRPM2 in the regulation of inhibitory synaptic strength and reveal Ca^{2+} and CaMKII as the most plausible downstream mediators. Consistent with this, other work supports TRPM2 as the Ca^{2+} source for CaMKII activity in the context of cell cycle regulation (Wang et al., 2017; Cai et al., 2023), suggesting this may be a common mechanism across multiple cellular functions. Moreover, our BAPTA data indicate that continuous Ca^{2+} stimulus is required for enhanced sIPSC amplitude, a mechanism likely mediated by ongoing CaMKII activation downstream of TRPM2-Ca^{2+} influx (Fig. 8*A*,*B*). Notably, a prominent property of the TRPM2 channel is its ability to conduct substantial Ca^{2+} current due to its high Ca^{2+} permeability and prolonged open time of several hundred milliseconds (Perraud et al., 2001; Sano et al., 2001; Kraft et al., 2004). Nonetheless, more work directly linking TRPM2-Ca^{2+} influx upstream of CaMKII activation should be a priority for future investigation but remains technically challenging due to the lack of reliable antibodies

directed at the channel (Dietz et al., 2020) and the poorly understood mechanism by which the channel is activated within the postsynaptic microdomain.

The Ca^{2+}-activated signaling cascade downstream of TRPM2 ion channel activation is important to elucidate both for increased understanding of the mechanism of ischemia-induced alterations in E/I balance as well as future therapeutic development. Using two distinct pharmacological inhibitors of CaMKII, our data show that Ca^{2+}-stimulated CaMKII activity is required for the elevation in postsynaptic GABAergic inhibition following GCI. Specifically, treatment with KN93, an inhibitor known to preferentially block Ca^{2+}-dependent CaMKII (Vest et al., 2010), occluded the OGD effect on clustering (Fig. 9*F,G*). Consistent with this, we find that the tatCN19o peptide, which blocks both stimulated and autonomous CaMKII activity (Vest et al., 2010), also reduced the OGD effect on postsynaptic GABAergic clustering (Fig. 9*C,D*) and the CA/CPR-induced increase in sIPSC amplitude (Fig. 8F_1). Thus, we cannot exclude the involvement of autonomous CaMKII in this mechanism. These data agree with the literature implicating CaMKII in inhibitory synaptic potentiation. Autonomous CaMKII (T286phosphorylated) constitutively localizes to inhibitory synapses (Marsden et al., 2010; Cook et al., 2022), and intracellular application of CaMKII was shown to enhance GABA IPSCs (Wang et al., 1995; Wei et al., 2004). Following its movement to inhibitory synapses, CaMKII was shown to phosphorylate b2 or b3 subunits of $GABA_A$Rs, resulting in $GABA_A$R synaptic aggregation and inhibitory potentiation (Petrini et al., 2014; Chiu et al., 2018). Exploring whether CaMKII moves to inhibitory synapses and directly phosphorylates GABAergic proteins to alter E/I balance after ischemia is an important avenue for future investigation. One caveat to targeting CaMKII to restore ischemia-induced E/I imbalance is its well-established role in mediating AMPA receptor currents (Kristensen et al., 2011). Thus, both excitatory and inhibitory signaling would likely be affected by CaMKII inhibition. To mitigate the effect of CaMKII activation on excitatory transmission, future work should consider precise targeting of its impact on inhibitory synapses, potentially through blockade of its potential GABAergic phosphorylation sites.

Accumulating evidence suggests inhibitory LTP and homeostatic scaling up share downstream signaling pathways to regulate synaptic strength (Vitureira and Goda, 2013; Galanis and Vlachos, 2020). Exocytosis and subsequent lateral diffusion of $GABA_A$Rs from the extrasynaptic membrane is a well-documented mechanism for rapidly fine-tuning inhibitory synaptic strength (Luscher et al., 2011). Multiple findings here support the notion that $GABA_A$R clustering is increased through lateral diffusion. First, our data demonstrate that sIPSC amplitude and $GABA_A$R clustering can be restored rapidly (within minutes to 1 h). Second, we observe unaltered mRNA expression of $GABA_A$R transcripts and protein levels of gephyrin post-CA/CPR, indicating no changes in the transcription and translation of GABAergic components at this timepoint. Lastly, our findings raise the intriguing possibility that increased inhibitory synaptic function represents a maladaptive homeostatic response to the acute loss of inhibition following excitotoxic insult. The OGD reoxygenation data hints at this possibility, revealing an initial acute reduction in the clustering of GABAergic components, followed by a steadily increasing and sustained increase in GABAergic synapses at later timepoints.

In summary, this study uncovers a novel mechanism whereby enhanced GABAergic inhibition impairs excitatory synaptic plasticity in the context of cerebral ischemia, revealing TRPM2 and CaMKII as targets for pharmacological intervention. This is particularly significant given the clinical challenges associated with direct $GABA_A$R modulation. $GABA_A$R antagonism induces epileptic seizures (Sperk et al., 2004), while $GABA_A$R agonists largely failed in clinical trials as a treatment for acute ischemic stroke due to lack of efficacy and patients reporting numerous problematic side effects (Wahlgren et al., 2000; Lyden et al., 2002; Liu et al., 2018). Furthermore, our data shed light on the temporal changes in inhibitory synaptic function in response to ischemic insult. This observation may have a profound impact on the therapeutic window of some interventions, particularly GABA agonists, which have been shown to confer neuroprotection in animal models acutely (Liu et al., 2010, 2018) but, in light of this data, may be detrimental to functional recovery if administered at more chronic timepoints. Beyond ischemic injury, the pathway described here likely has broader implications considering that disruptions in synaptic accumulation of $GABA_A$Rs are linked to numerous central nervous system disorders (Jacob et al., 2008; Mele et al., 2019). Further research into the precise molecular and cellular mechanisms underlying the influence of enhanced postsynaptic GABAergic function on excitatory LTP will be pivotal in developing targeted interventions to mitigate the long-term cognitive deficits associated with cerebral ischemia and various neurological diseases.

References

Alicke B, Schwartz-Bloom RD (1995) Rapid down-regulation of GABAA receptors in the gerbil hippocampus following transient cerebral ischemia. J Neurochem 65:2808–2811.

Arancibia-Carcamo IL, Yuen EY, Muir J, Lumb MJ, Michels G, Saliba RS, Smart TG, Yan Z, Kittler JT, Moss SJ (2009) Ubiquitin-dependent lysosomal targeting of GABA(A) receptors regulates neuronal inhibition. Proc Natl Acad Sci U S A 106:17552–17557.

Azad TD, Veeravagu A, Steinberg GK (2016) Neurorestoration after stroke. Neurosurg Focus 40:E2.

Banks MI, Li TB, Pearce RA (1998) The synaptic basis of GABAA, slow. J Neurosci 18:1305–1317.

Barcomb K, Goodell DJ, Arnold DB, Bayer KU (2015) Live imaging of endogenous Ca(2)(+)/calmodulin-dependent protein kinase II in neurons reveals that ischemia-related aggregation does not require kinase activity. J Neurochem 135:666–673.

Cai X, et al. (2023) TRPM2 regulates cell cycle through the Ca2+-CaM-CaMKII signaling pathway to promote HCC. Hepatol Commun 7:e0101.

Carmichael ST (2012) Brain excitability in stroke: the yin and yang of stroke progression. Arch Neurol 69:161–167.

Cheng YD, Al-Khoury L, Zivin JA (2004) Neuroprotection for ischemic stroke: two decades of success and failure. NeuroRx 1:36–45.

Chiu CQ, Barberis A, Higley MJ (2019) Preserving the balance: diverse forms of long-term GABAergic synaptic plasticity. Nat Rev Neurosci 20:272–281.

Chiu CQ, Martenson JS, Yamazaki M, Natsume R, Sakimura K, Tomita S, Tavalin SJ, Higley MJ (2018) Input-specific NMDAR-dependent potentiation of dendritic GABAergic inhibition. Neuron 97:368–377.e3.

Clarkson AN, Huang BS, Macisaac SE, Mody I, Carmichael ST (2010) Reducing excessive GABA-mediated tonic inhibition promotes functional recovery after stroke. Nature 468:305–309.

Cook SG, Buonarati OR, Coultrap SJ, Bayer KU (2021) CaMKII holoenzyme mechanisms that govern the LTP versus LTD decision. Sci Adv 7: eabe2300.

Cook SG, Rumian NL, Bayer KU (2022) CaMKII T286 phosphorylation has distinct essential functions in three forms of long-term plasticity. J Biol Chem 298:102299.

Costa AC, Grybko MJ (2005) Deficits in hippocampal CA1 LTP induced by TBS but not HFS in the Ts65Dn mouse: a model of Down syndrome. Neurosci Lett 382:317–322.

Costa JT, Mele M, Baptista MS, Gomes JR, Ruscher K, Nobre RJ, de Almeida LP, Wieloch T, Duarte CB (2016) Gephyrin cleavage in in vitro brain

ischemia decreases GABAA receptor clustering and contributes to neuronal death. Mol Neurobiol 53:3513–3527.
Crosby KC, Gookin SE, Garcia JD, Hahm KM, Dell'Acqua ML, Smith KR (2019) Nanoscale subsynaptic domains underlie the organization of the inhibitory synapse. Cell Rep 26:3284–3297.e3.
Cruz-Torres I, Backos DS, Herson PS (2020) Characterization and optimization of the novel transient receptor potential melastatin 2 antagonist tatM2NX. Mol Pharmacol 97:102–111.
Deng G, Orfila JE, Dietz RM, Moreno-Garcia M, Rodgers KM, Coultrap SJ, Quillinan N, Traystman RJ, Bayer KU, Herson PS (2017) Autonomous CaMKII activity as a drug target for histological and functional neuroprotection after resuscitation from cardiac arrest. Cell Rep 18:1109–1117.
Dietz RM, Cruz-Torres I, Orfila JE, Patsos OP, Shimizu K, Chalmers N, Deng G, Tiemeier E, Quillinan N, Herson PS (2020) Reversal of global ischemia-induced cognitive dysfunction by delayed inhibition of TRPM2 ion channels. Transl Stroke Res 11:254–266.
Dietz RM, Orfila JE, Chalmers N, Minjarez C, Vigil J, Deng G, Quillinan N, Herson PS (2021) Functional restoration following global cerebral ischemia in juvenile mice following inhibition of transient receptor potential M2 (TRPM2) ion channels. Neural Plast 2021:8774663.
Escobar I, Xu J, Jackson CW, Perez-Pinzon MA (2019) Altered neural networks in the Papez circuit: implications for cognitive dysfunction after cerebral ischemia. J Alzheimers Dis 67:425–446.
Galanis C, Vlachos A (2020) Hebbian and homeostatic synaptic plasticity-do alterations of one reflect enhancement of the other? Front Cell Neurosci 14:50.
Garcia JD, Gookin SE, Crosby KC, Schwartz SL, Tiemeier E, Kennedy MJ, Dell'Acqua ML, Herson PS, Quillinan N, Smith KR (2021) Stepwise disassembly of GABAergic synapses during pathogenic excitotoxicity. Cell Rep 37:110142.
Hill K, McNulty S, Randall AD (2004) Inhibition of TRPM2 channels by the antifungal agents clotrimazole and econazole. Naunyn Schmiedebergs Arch Pharmacol 370:227–237.
Hiu T, et al. (2016) Enhanced phasic GABA inhibition during the repair phase of stroke: a novel therapeutic target. Brain 139:468–480.
Jacob TC, Moss SJ, Jurd R (2008) GABA(a) receptor trafficking and its role in the dynamic modulation of neuronal inhibition. Nat Rev Neurosci 9:331–343.
Jia J, Verma S, Nakayama S, Quillinan N, Grafe MR, Hurn PD, Herson PS (2011) Sex differences in neuroprotection provided by inhibition of TRPM2 channels following experimental stroke. J Cereb Blood Flow Metab 31:2160–2168.
Joy MT, Carmichael ST (2021) Encouraging an excitable brain state: mechanisms of brain repair in stroke. Nat Rev Neurosci 22:38–53.
Katz A, Brosnahan SB, Papadopoulos J, Parnia S, Lam JQ (2022) Pharmacologic neuroprotection in ischemic brain injury after cardiac arrest. Ann N Y Acad Sci 1507:49–59.
Kostandy BB (2012) The role of glutamate in neuronal ischemic injury: the role of spark in fire. Neurol Sci 33:223–237.
Kraft R, Grimm C, Grosse K, Hoffmann A, Sauerbruch S, Kettenmann H, Schultz G, Harteneck C (2004) Hydrogen peroxide and ADP-ribose induce TRPM2-mediated calcium influx and cation currents in microglia. Am J Physiol Cell Physiol 286:C129–C137.
Kristensen AS, Jenkins MA, Banke TG, Schousboe A, Makino Y, Johnson RC, Huganir R, Traynelis SF (2011) Mechanism of Ca2+/calmodulin-dependent kinase II regulation of AMPA receptor gating. Nat Neurosci 14:727–735.
Lake EM, Chaudhuri J, Thomason L, Janik R, Ganguly M, Brown M, McLaurin J, Corbett D, Stanisz GJ, Stefanovic B (2015) The effects of delayed reduction of tonic inhibition on ischemic lesion and sensorimotor function. J Cereb Blood Flow Metab 35:1601–1609.
Leao RN, et al. (2012) OLM interneurons differentially modulate CA3 and entorhinal inputs to hippocampal CA1 neurons. Nat Neurosci 15:1524–1530.
Liu B, et al. (2010) Preservation of GABAA receptor function by PTEN inhibition protects against neuronal death in ischemic stroke. Stroke 41:1018–1026.
Liu J, Zhang J, Wang LN (2018) Gamma aminobutyric acid (GABA) receptor agonists for acute stroke. Cochrane Database Syst Rev 10:CD009622.
Luscher B, Fuchs T, Kilpatrick CL (2011) GABAA receptor trafficking-mediated plasticity of inhibitory synapses. Neuron 70:385–409.
Lyden P, et al. (2002) Clomethiazole acute stroke study in ischemic stroke (CLASS-I): final results. Stroke 33:122–128.
Marsden KC, Shemesh A, Bayer KU, Carroll RC (2010) Selective translocation of Ca2+/calmodulin protein kinase IIalpha (CaMKIIalpha) to inhibitory synapses. Proc Natl Acad Sci U S A 107:20559–20564.
Mele M, Costa RO, Duarte CB (2019) Alterations in GABA(A)-receptor trafficking and synaptic dysfunction in brain disorders. Front Cell Neurosci 13:77.
Mele M, Ribeiro L, Inacio AR, Wieloch T, Duarte CB (2014) GABA(A) receptor dephosphorylation followed by internalization is coupled to neuronal death in in vitro ischemia. Neurobiol Dis 65:220–232.
Nakayama S, Vest R, Traystman RJ, Herson PS (2013) Sexually dimorphic response of TRPM2 inhibition following cardiac arrest-induced global cerebral ischemia in mice. J Mol Neurosci 51:92–98.
Neumann JT, Cohan CH, Dave KR, Wright CB, Perez-Pinzon MA (2013) Global cerebral ischemia: synaptic and cognitive dysfunction. Curr Drug Targets 14:20–35.
Orfila JE, et al. (2019) Delayed inhibition of tonic inhibition enhances functional recovery following experimental ischemic stroke. J Cereb Blood Flow Metab 39:1005–1014.
Orfila JE, McKinnon N, Moreno M, Deng G, Chalmers N, Dietz RM, Herson PS, Quillinan N (2018) Cardiac arrest induces ischemic long-term potentiation of hippocampal CA1 neurons that occludes physiological long-term potentiation. Neural Plast 2018:9275239.
Orfila JE, Shimizu K, Garske AK, Deng G, Maylie J, Traystman RJ, Quillinan N, Adelman JP, Herson PS (2014) Increasing small conductance Ca2+-activated potassium channel activity reverses ischemia-induced impairment of long-term potentiation. Eur J Neurosci 40:3179–3188.
Perraud AL, et al. (2001) ADP-ribose gating of the calcium-permeable LTRPC2 channel revealed by Nudix motif homology. Nature 411:595–599.
Petito CK, Feldmann E, Pulsinelli WA, Plum F (1987) Delayed hippocampal damage in humans following cardiorespiratory arrest. Neurology 37:1281–1286.
Petrini EM, et al. (2014) Synaptic recruitment of gephyrin regulates surface GABAA receptor dynamics for the expression of inhibitory LTP. Nat Commun 5:3921.
Rajgor D, Purkey AM, Sanderson JL, Welle TM, Garcia JD, Dell'Acqua ML, Smith KR (2020) Local miRNA-dependent translational control of GABA(A)R synthesis during inhibitory long-term potentiation. Cell Rep 31:107785.
Sano Y, Inamura K, Miyake A, Mochizuki S, Yokoi H, Matsushime H, Furuichi K (2001) Immunocyte Ca2+influx system mediated by LTRPC2. Science 293:1327–1330.
Schmidt-Kastner R, Freund TF (1991) Selective vulnerability of the hippocampus in brain ischemia. Neuroscience 40:599–636.
Schwartz-Bloom RD, Sah R (2001) Gamma-aminobutyric acid(a) neurotransmission and cerebral ischemia. J Neurochem 77:353–371.
Shimizu T, Macey TA, Quillinan N, Klawitter J, Perraud AL, Traystman RJ, Herson PS (2013) Androgen and PARP-1 regulation of TRPM2 channels after ischemic injury. J Cereb Blood Flow Metab 33:1549–1555.
Smith KR, Kittler JT (2010) The cell biology of synaptic inhibition in health and disease. Curr Opin Neurobiol 20:550–556.
Smith KR, Muir J, Rao Y, Browarski M, Gruenig MC, Sheehan DF, Haucke V, Kittler JT (2012) Stabilization of GABA(A) receptors at endocytic zones is mediated by an AP2 binding motif within the GABA(A) receptor beta3 subunit. J Neurosci 32:2485–2498.
Smith KR, Rajgor D, Hanley JG (2017) Differential regulation of the Rac1 GTPase-activating protein (GAP) BCR during oxygen/glucose deprivation in hippocampal and cortical neurons. J Biol Chem 292:20173–20183.
Sperk G, Furtinger S, Schwarzer C, Pirker S (2004) GABA and its receptors in epilepsy. Adv Exp Med Biol 548:92–103.
Steele PM, Mauk MD (1999) Inhibitory control of LTP and LTD: stability of synapse strength. J Neurophysiol 81:1559–1566.
Turski L, Huth A, Sheardown M, McDonald F, Neuhaus R, Schneider HH, Dirnagl U, Wiegand F, Jacobsen P, Ottow E (1998) ZK200775: a phosphonate quinoxalinedione AMPA antagonist for neuroprotection in stroke and trauma. Proc Natl Acad Sci U S A 95:10960–10965.
Udakis M, Pedrosa V, Chamberlain SEL, Clopath C, Mellor JR (2020) Interneuron-specific plasticity at parvalbumin and somatostatin inhibitory synapses onto CA1 pyramidal neurons shapes hippocampal output. Nat Commun 11:4395.

Verma S, Quillinan N, Yang YF, Nakayama S, Cheng J, Kelley MH, Herson PS (2012) TRPM2 channel activation following in vitro ischemia contributes to male hippocampal cell death. Neurosci Lett 530:41–46.

Vest RS, O'Leary H, Coultrap SJ, Kindy MS, Bayer KU (2010) Effective post-insult neuroprotection by a novel Ca(2+)/calmodulin-dependent protein kinase II (CaMKII) inhibitor. J Biol Chem 285:20675–20682.

Vitureira N, Goda Y (2013) Cell biology in neuroscience: the interplay between Hebbian and homeostatic synaptic plasticity. J Cell Biol 203:175–186.

Vogels TP, Sprekeler H, Zenke F, Clopath C, Gerstner W (2011) Inhibitory plasticity balances excitation and inhibition in sensory pathways and memory networks. Science 334:1569–1573.

Wahlgren NG, Ahmed N (2004) Neuroprotection in cerebral ischaemia: facts and fancies–the need for new approaches. Cerebrovasc Dis 17:153–166.

Wahlgren NG, Matias-Guiu J, Lainez JM, Veloso F, Ranasinha K, Grossman E, Ashwood T, CLASS Study Group (2000) The clomethiazole acute stroke study (CLASS): safety results in 1,356 patients with acute hemispheric stroke. J Stroke Cerebrovasc Dis 9:158–165.

Walters MR, Kaste M, Lees KR, Diener HC, Hommel M, De Keyser J, Steiner H, Versavel M (2005) The AMPA antagonist ZK 200775 in patients with acute ischaemic stroke: a double-blind, multicentre, placebo-controlled safety and tolerability study. Cerebrovasc Dis 20:304–309.

Wang RA, Cheng G, Kolaj M, Randic M (1995) Alpha-subunit of calcium/calmodulin-dependent protein kinase II enhances gamma-aminobutyric acid and inhibitory synaptic responses of rat neurons in vitro. J Neurophysiol 73:2099–2106.

Wang Q, Huang L, Yue J (2017) Oxidative stress activates the TRPM2-Ca(2+)-CaMKII-ROS signaling loop to induce cell death in cancer cells. Biochim Biophys Acta Mol Cell Res 1864:957–967.

Wei J, Zhang M, Zhu Y, Wang JH (2004) Ca(2+)-calmodulin signalling pathway up-regulates GABA synaptic transmission through cytoskeleton-mediated mechanisms. Neuroscience 127:637–647.

Williams LE, Holtmaat A (2019) Higher-order thalamocortical inputs gate synaptic long-term potentiation via disinhibition. Neuron 101:91–102.e4.

Wu QJ, Tymianski M (2018) Targeting NMDA receptors in stroke: new hope in neuroprotection. Mol Brain 11:15.

Xie YF, Belrose JC, Lei G, Tymianski M, Mori Y, Macdonald JF, Jackson MF (2011) Dependence of NMDA/GSK-3beta mediated metaplasticity on TRPM2 channels at hippocampal CA3-CA1 synapses. Mol Brain 4:44.